Acta Oceanol. Sin., 2019, Vol. 38, No. 5, P. 32–50
https://doi.org/10.1007/s13131-019-1439-x
http://www.hyxb.org.cn
E-mail: hyxbe@263.net

Upper ocean high resolution regional modeling of the Arabian Sea and Bay of Bengal

Dwivedi Suneet[1]*, Mishra Alok Kumar[1], Srivastava Atul[1]

[1] K Banerjee Centre of Atmospheric and Ocean Studies and M N Saha Centre of Space Studies, University of Allahabad, Allahabad UP 211002, India

Received 6 December 2017; accepted 26 February 2018

© Chinese Society for Oceanography and Springer-Verlag GmbH Germany, part of Springer Nature 2019

Abstract

In this paper, effort is made to demonstrate the quality of high-resolution regional ocean circulation model in realistically simulating the circulation and variability properties of the northern Indian Ocean (10°S–25°N, 45°–100°E) covering the Arabian Sea (AS) and Bay of Bengal (BoB). The model run using the open boundary conditions is carried out at 10 km horizontal resolution and highest vertical resolution of 2 m in the upper ocean. The surface and sub-surface structure of hydrographic variables (temperature and salinity) and currents is compared against the observations during 1998–2014 (17 years). In particular, the seasonal variability of the sea surface temperature, sea surface salinity, and surface currents over the model domain is studied. The high-resolution model's ability in correct estimation of the spatio-temporal mixed layer depth (MLD) variability of the AS and BoB is also shown. The lowest MLD values are observed during spring (March-April-May) and highest during winter (December-January-February) seasons. The maximum MLD in the AS (BoB) during December to February reaches 150 m (67 m). On the other hand, the minimum MLD in these regions during March-April-May becomes as low as 11–12 m. The influence of wind stress, net heat flux and freshwater flux on the seasonal variability of the MLD is discussed. The physical processes controlling the seasonal cycle of sea surface temperature are investigated by carrying out mixed layer heat budget analysis. It is found that air-sea fluxes play a dominant role in the seasonal evolution of sea surface temperature of the northern Indian Ocean and the contribution of horizontal advection, vertical entrainment and diffusion processes is small. The upper ocean zonal and meridional volume transport across different sections in the AS and BoB is also computed. The seasonal variability of the transports is studied in the context of monsoonal currents.

Key words: Indian Ocean modeling, Arabian Sea and Bay of Bengal, mixed layer depth, transport

Citation: Suneet Dwivedi, Alok Kumar Mishra, Atul Srivastava. 2019. Upper ocean high resolution regional modeling of the Arabian Sea and Bay of Bengal. Acta Oceanologica Sinica, 38(5): 32–50, doi: 10.1007/s13131-019-1439-x

1 Introduction

Understanding the Arabian Sea (AS) and Bay of Bengal (BoB) circulation and the variability of the Indian Ocean exhibits on different time scales (seasonal, interannual, decadal and longer) is very important for the Indian subcontinent. The better understanding of the AS and BoB circulation and variability of the surface and sub-surface variables shall not only help in the improvement of forecasting of the Indian summer monsoon rainfall and tropical cyclones (Dube et al., 1990; Achuthavarier et al., 2012; Subrahmanyam et al., 2005; Ali et al., 2015; Vinayachandran et al., 2015) but it will also have a potential positive impact on the economy of the regions surrounding the ocean. Moreover, the variability in the hydrography and circulation of the AS and BoB also influences and gets influenced by the tropical Pacific interannual variability (Gutzler and Harrison, 1987; Annamalai et al., 2005; Schott et al., 2009 and references therein), and the monsoons over East Africa, and Australia (Annamalai and Murtugudde, 2004; Vecchi and Harrison, 2004; Song et al., 2007).

The Indian Ocean circulation is greatly influenced by the near surface air-sea forcings (Schott and McCreary, 2001; Callaghan et al., 2014; Vinayachandran et al., 2015). The circulation is generally considered to be wind and buoyancy driven (Liu and Alexander, 2007). The air-sea interaction processes (including Indian summer monsoon rainfall), wind stress, heat and freshwater flux strongly impact AS and BoB circulation. The AS and BoB circulation, on the other hand, influences the Indian summer monsoon rainfall (Roxy et al., 2015; Krishnamurthy and Kirtman, 2003; Wu and Kirtman, 2004 and references therein). It is, therfore, important to understand the impact of air-sea forcings on the quality of the ocean circulation model output. Several researchers have carried out sensitivity studies for this purpose in the AS and BoB using different air-sea forcing products (Wajsowicz, 2002; Prasad, 2004; Agarwal et al., 2007; Sharma et al., 2007; Chakraborty et al., 2014). However, none of these studies have focused on understanding the relative roles of wind and buoyancy forcings on the mixed layer depth variability of the region using 3-D high-resolution model output. One of the aims of this study is, therefore, to decipher the relative roles of interannually varying winds, heat and freshwater flux forcings in influencing the AS and BoB mixed layer depth variability at eddy-resolving scales. Moreover, the spatio-temporal mixed layer heat budget (Huang et al., 2010, 2012; Foltz et al., 2003) analysis of the northern Indian Ocean using long term high-resolution model output is also not available even though it is important for investigating the processes that control the seasonal cycle of seasurface temperature in the northern Indian Ocean (Thangaprakash et al., 2016 and refer-

*Corresponding author, E-mail: suneetdwivedi@gmail.com

ences therein). In the present manuscript, we, therefore, also make an attempt to quantify the mixed layer heat budget using our model output and estimate the relative contributions coming from surface fluxes, advection, diffusion, and entrainment terms.

Various observational and ocean circulation modeling studies have been performed in the recent past in the region surrounding the AS and BoB. Sharma et al. (2007, 2010, 2012) studied the sea surface salinity (SSS) variability in the tropical Indian Ocean using an ocean general circulation model (OGCM). Kantha et al. (2008) simulated the North Indian Ocean circulation and variability for the period 1993–2004. Rao and Sivakumar (2003) used observations to explain the seasonal variability of SSS and mixed layer salt budget in the AS and BoB. Thadathil et al. (2002) studied various aspects of the surface layer temperature inversion in the BoB. Vinayachandran and Kurian (2007) investigated the low salinity regimes during the summer monsoon in the western BoB. Schott and McCreary (2001) presented an in-depth review on the monsoon circulation of the Indian Ocean. Prasanna Kumar and Narvekar (2005) studied mixed layer depth seasonal variability and its implication to nutrients and primary productivity in the central AS. The mixed layer depth variability in the central BoB and associated changes in nutrients and chlorophyll was examined by Narvekar and Prasanna Kumar (2006). Shenoi et al. (1999) and Shankar et al. (2002) explained tropical Indian Ocean surface circulation using long-term ocean observations. Thompson et al. (2006, 2008) used ocean model to understand the variability of the Indian Ocean circulation and salinity. Han et al. (2001) examined how salinity distributions in the BoB affect dynamics, thermodynamics, and mixed layer physics in the upper Indian Ocean. Durand et al. (2007) investigated the effect of salinity on the formation of the barrier layer in the southeastern Arabian Sea (SEAS). Durand et al. (2011) used an ocean model to study the impact of monthly Ganges-Brahmaputra river discharge variations on the BoB salinity and temperature. Similarly, de Boyer Montégut et al. (2014) examined the role of salinity fronts on the spatio-temporal structure of the AS barrier layers during summer monsoon season. Akhil et al. (2014) studied the processes responsible for strong SSS seasonal cycle in the BoB.

One of the main reasons behind the incomplete understanding of the AS and BoB circulation and variability is the limited availability of the high-resolution (surface and subsurface) data of the oceanographic variables (of hydrography and velocity) in space and time. The availability of such data is also important in realistic estimation of the ocean heat content, mixed layer depth, and volume transport. The correct knowledge of these on the other hand is very important from the point of view of biological production and source-sink of carbon containing gases (Bates 2006a, b). The satellite dataset is limited to surface variables only and the *in situ* (depth dependent) observations are a few. The recourse is taken in this case by running high-resolution OGCMs in a limited area (AS and BoB of the Indian Ocean, for example) and validating the model results against the available observations. The OGCMs offer themselves as a powerful tool for this purpose and help in generating 3-dimensional time varying oceanic fields at desired resolutions. However, examples of such studies which have focused on understanding the Indian Ocean variability at eddy-resolving scales of O (10 km) are a few. Wu et al. (2007) have used an eddy-resolving OGCM to investigate the evolution of freshwater plumes and salinity fronts in the northern BoB. Using the altimetry data and an eddy-resolving ocean model Cheng et al. (2013) examined the intraseasonal variability of sea surface height over the BoB. Diansky et al. (2006) studied the monsoon circulation in the Indian Ocean using a high-resolution σ-coordinate ocean model. Huang et al. (2015) used a (1/8)° coupled biochemical-physical Indian Ocean Regional Model to provide an estimate of the oceanic physical state along with the biochemical processes in the Indian Ocean. Masumoto et al. (2008) and George et al. (2010) demonstrated the advantage of using eddy-permitting ocean model for the Indian Ocean towards the simulation of major surface and subsurface variables. Momin et al. (2014) have also argued for higher horizontal resolution in their Indian Ocean intercomparison study, though their model resolution was still too coarse. Similarly, Vinayachandran et al. (1996) also showed the usefulness of ocean models with higher horizontal resolution in better simulation of the BoB circulation. Benshila et al. (2014) demonstrated the advantage of high-resolution modeling studies in investigating the seasonal structure of sea surface salinity of the BoB.

However, none of these high-resolution studies have focused on the evolution of surface and subsurface hydrography (temperature, and salinity), and circulation (velocity) of AS and BoB together over a longer duration of time (which also takes into account concomitant effect of climate change in recent decades, for example). In addition to this, seasonal variability of the mixed layer depth of the AS and BoB and its relation to monsoonal currents has not been studied in detail using high-resolution model data. Moreover, reliable estimates of the transport of water mass from AS to BoB and vice versa and the associated changes during summer and winter monsoon seasons are also not present due to lack to quality-controlled high resolution dataset. Another major objective of this study is, therefore, to perform high-resolution (10 km) ocean circulation modeling in the Indian Ocean surrounding the AS and BoB regions during 1998–2014. The model results are compared and contrasted against the available ocean observations. The reliable estimates of hydrography, circulation, mixed layer depth, and volume transport (zonal and meridional) are obtained.

The paper is organized as follows. Section 2 gives a brief account of the ocean circulation model configuration. The results and discussion are given in Section 3. The quality of the model output, the spatio-temporal variability of the mixed layer depth, the mixed layer heat budget analysis, and the quantification of volume transports are given in this section. Conclusions are in Section 4.

2 Model configuration

The ocean circulation model MITgcm (Marshall et al., 1997) is configured to run at a horizontal resolution of 10 km around the region (10°S–25°N, 45°–100°E) in the northern Indian Ocean. The MITgcm is a z-coordinate model and solves the incompressible Navier-Stokes equation. The Boussinesq and hydrostatic approximations are used here. We use 36 levels in the vertical (Table 1) with highest resolution of 2 m near the surface and then slowing telescoping out at depth. To represent the sub-grid scale mixing in vertical, we use K-profile parameterization (KPP) scheme (Large et al., 1994). The bathymetry of the model (Fig. 1) is derived from the high-resolution (1′) topography data of Smith and Sandwell (1997). The eddy (harmonic) viscosity and diffusivity are chosen in horizontal and vertical. The model uses no-slip condition on sides as well as bottom. The bottom frictional drag coefficient is taken as 0.001. A third order direct space-time advection scheme is employed for temperature and salinity. The nonlinear equation of state is used following Jackett and McDougall (1995). The model is forced by the 6-hourly NCEP/NCAR reanalysis (Kalnay et al., 1996) air temperature, relative humidity,

Table 1. Depth of vertical levels in the model

Level	Depth/m
1	2
2	2
3	2
4	2
5	2
6	3
7	3
8	3
9	3
10	3
11	4
12	4
13	4
14	5
15	5
16	6
17	8
18	10
19	13
20	17
21	22
22	28
23	35
24	45
25	55
26	70
27	90
28	130
29	190
30	250
31	350
32	450
33	500
34	500
35	600
36	600

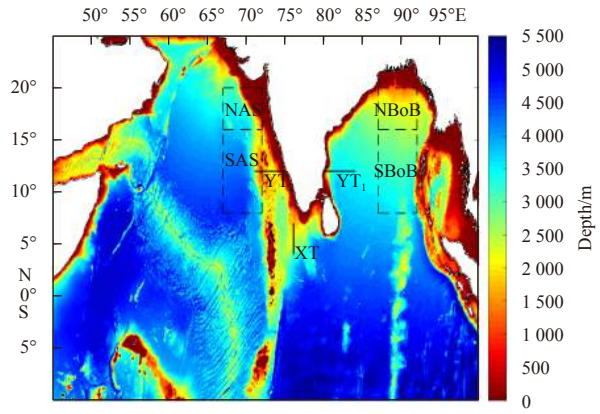

Fig. 1. Bathymetry of the northern Indian Ocean around (10°S–25°N, 45°–100°E). The horizontal lines in the Arabian Sea and Bay of Bengal represent sections along which meridional volume transport is computed. The vertical line at the interface of Arabian Sea and Bay of Bengal represents section along which zonal volume transport is computed.

downward long-wave and short-wave radiation, precipitation, runoff, zonal and meridional wind data. The model calculates the air-sea fluxes, namely, ocean surface wind stress, and heat flux from these prescribed atmospheric states (interpolated to model grid) using the bulk formulae (Large and Pond, 1982). The freshwater flux is computed as evaporation minus precipitation minus runoff. The model uses the open boundary conditions on all the sides. The values of temperature, salinity, zonal and meridional velocity prescribed at each boundary are extracted from the ocean reanalysis system 4 (ORAS4) (Balmaseda et al., 2013). The boundary values are updated at an interval of 30 d. The model computes net flow across the boundaries and adjusts all normal velocities on boundaries to obtain zero net inflow. The model's surface salinity is relaxed towards monthly climatology with a time scale of 30 d (Li et al., 2015). The model is spun-up for five years (from 1 January 1993 to 31 December 1997) with the initial temperature and salinity values derived from the World Ocean Atlas 2013 (WOA13). The output of the model is stored on a daily basis. The various datasets described in this section are also summarized in Table 2.

3 Results and discussion

3.1 *Quality of the model output*

The MITgcm is customized to run over the Arabian Sea and Bay of Bengal regions of the northern Indian Ocean for 17 a from 1 January 1998 to 31 December 2014 using the setup described in Section 2. The model uses the initial temperature, salinity, sea level elevation, zonal and meridional velocity from the spin-up run. We show in Fig. 2 (upper panel) the climatological sea surface temperature (SST) from model over the region of study. The corresponding SST values from the TRMM Microwave Imager (TMI) (Wentz et al., 2015) are also shown in the figure. It is clear from the figure that the model is able to reasonably capture the mean state of the SST. The lowest SST values are observed in the western AS. The spatial correlation coefficient of the temporally averaged model SST with the corresponding TMI values is 0.91 (at 99.9% significance level). The SST bias (TMI-model) is also shown in the figure. We see from the figure that the bias is very small in most parts of the domain. The bias seen along the coasts, however, may be ignored since TMI has known problems along the coasts (Wang et al., 2011). The SST root mean square error (RMSE) between the annually averaged model and TMI is 0.35 °C which is much smaller than the standard deviation of 0.92 °C of the annually averaged TMI SST, thus confirming the quality of model output.

The climatological sea surface salinity (SSS) results are also shown in Fig. 2 (lower panel). The comparison of model SSS is made against the NIO Climatological Atlas (NIOA) (Chatterjee et al., 2012). The model realistically simulates high surface salinity values in the AS and low values in the BoB. The spatial correlation coefficient between the temporally averaged model SSS and the corresponding NIOA SSS is 0.95, with a significance level of 99.9%. The model shows small SSS bias with respect to NIOA in nearly all the regions except in the northern BoB. The RMSE between the annually averaged model and NIOA SSS is 0.36 which is much smaller than the standard deviation of 1.28 of the annually averaged NIOA SSS.

To make an assessment of the model's ability in capturing the spatio-temporal variability of the SST and SSS in the region of study, we compute their monthly and daily standard deviation from the model's data during 1 January 1998 to 31 December 2014 (Figs 3a and b, respectively). The corresponding monthly

Table 2. Dataset used in the model

Type	Data
Bathymetry	Smith and Sandwell (1997)
Initial condition	temperature and salinity from World Ocean Atlas 2013 (WOA13)
External forcing	6-hourly varying NCEP/NCAR reanalysis (Kalnay et al., 1996) air temperature, relative humidity, downward long-wave and short-wave radiation, precipitation, runoff, zonal and meridional wind data
Relaxation	SSS from the Ocean Reanalysis System 4 (ORAS4) (Balmaseda et al., 2013)
Open boundary Conditions	temperature, salinity, zonal and meridional velocity from the Ocean Reanalysis System 4 (ORAS4) (Balmaseda et al., 2013)

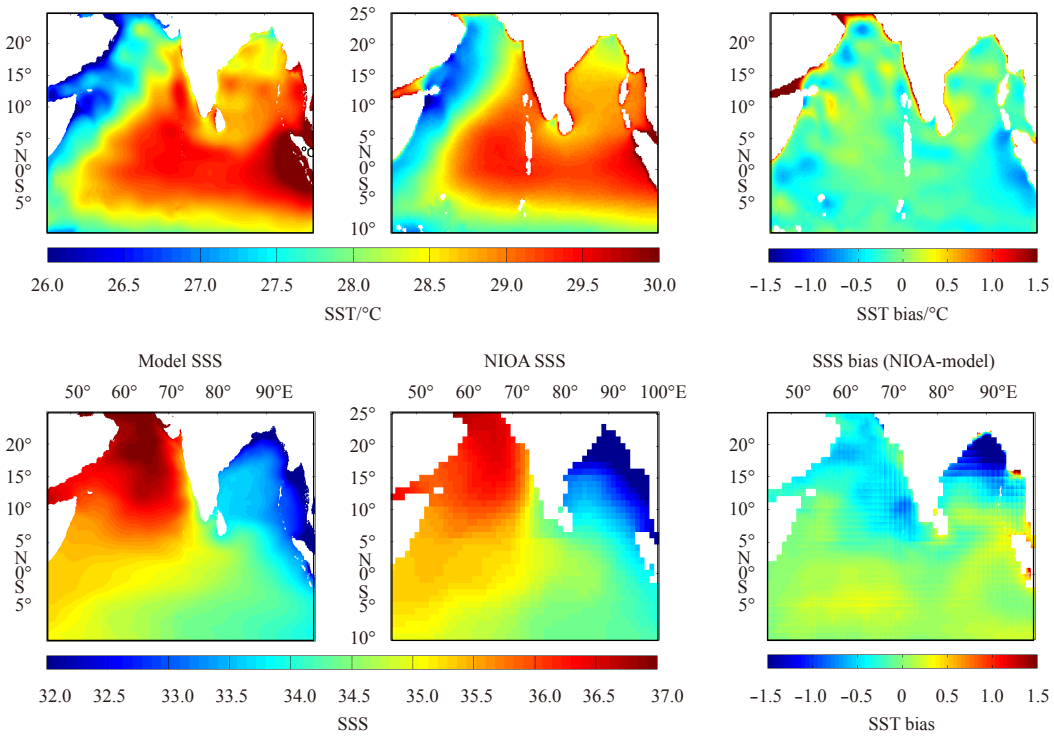

Fig. 2. Comparison of the climatological SST between model and TMI dataset during 1998–2014 (left upper panel); SST bias between Model and TMI SST (right upper panel); comparison of the climatological SSS between Model and NIOA dataset during 1998–2014 (left lower panel); and SSS bias between Model and NIOA SSS (right lower panel).

SST and SSS standard deviation values from the TMI and NIOA are shown in Fig. 3a, whereas, daily SST and SSS standard deviation values from the TMI and Aquarius (https://podaac.jpl.nasa.gov/aquarius; weekly values interpolated to daily values during 2012–2014) are shown in Fig. 3b. It is clear from the figures that barring a few places, the model is able to distinguish the region of high and low SST and SSS monthly and daily variability over the northern Indian Ocean domain covering the AS and BoB. Further, the daily variability of SST and SSS is always higher as compared to its monthly variability. The SST of the northern part of the domain is more variable as compared to the southern part. We also see from the figure that except western part of the model domain, the SST variability in general monotonically decreases from north to south. The northern BoB and AS show higher SST variablity compared to the southern portion. The SSS variability on the other hand, is higher in the southern AS as compared to northern AS. In the BoB, however, the northern region shows higher SSS variability. Nevertheless, except northern BoB and southern AS, all the other regions of the model domain exhibit very low SSS variability.

The surface and sub-surface variables in the AS and BoB exhibit significantly interesting changes at a seasonal scale (Rao and Sivakumar, 2003; de Boyer Montégut et al., 2007; Schott et al., 2009). Thus, the correct simulation of the seasonal variability of SST and SSS is very important. The cyclogenesis, and near-surface mixing properties in the AS and BoB are largely understood in terms of the seasonal variability of surface temperature and salinity (Neetu et al., 2012). We show in Fig. 4 the seasonal variability of the SST and compare it with the TMI SST and NIOA SST data. The seasonal averages are obtained for December-Januray-February, March-April-May, June-July-August, and September-October-November. We observe that the SST seasonal variability is very well capured by the model. The highest SST is obtained during spring months of March-April-May and lowest during the winter months of December-January-February, as expected. The northern BoB exhibits high SST values during June-July-August and September-October-November. This may happen primarily due to moderately high shortwave radiation compounded with shallow mixed layer depth as a result of increased freshwater flux and precipitation (see Section 3.2 below). Moreover, the creation of a barrier layer in the Bay of Bengal blocks heat transfer from surface to deep ocean. We also find that western and south-west-

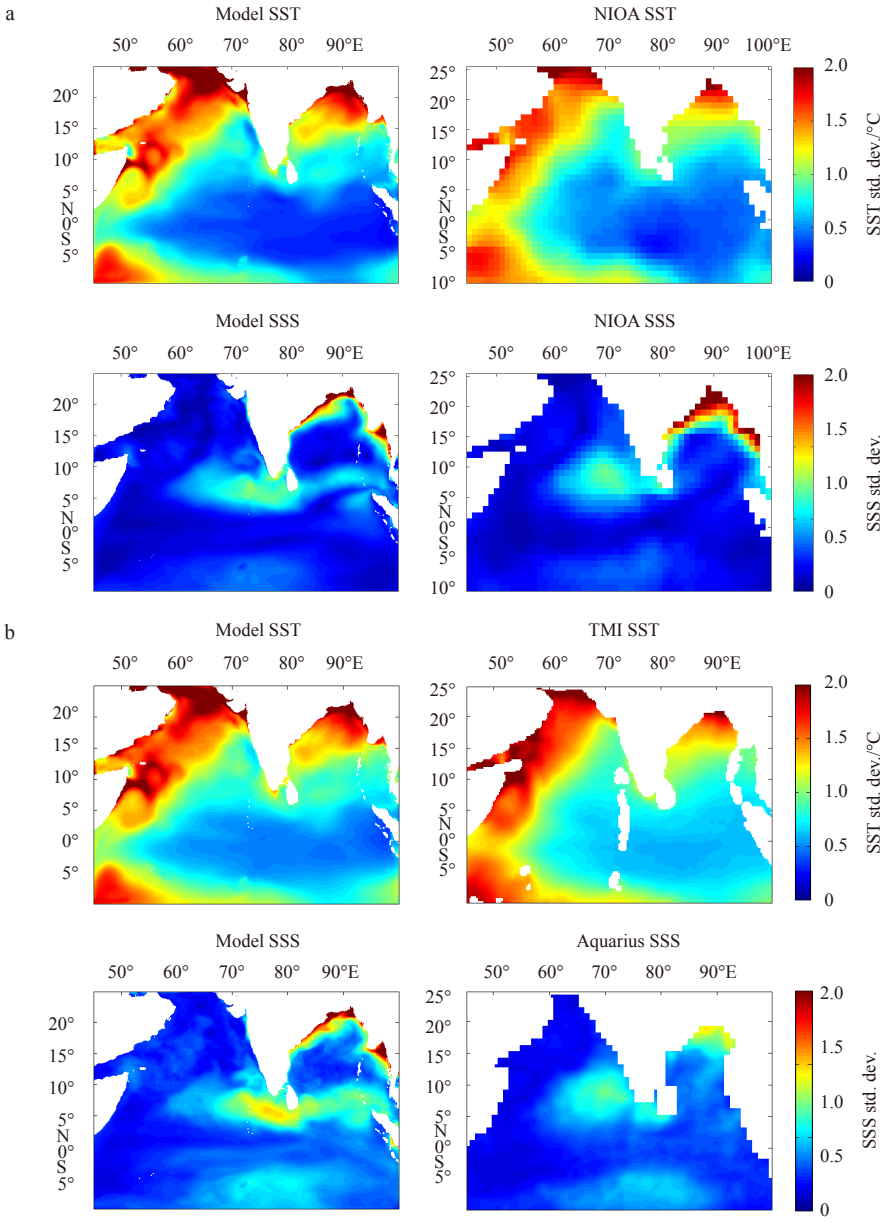

Fig. 3. Standard deviation (std. dev.) of the monthly SST from model and TMI (a, upper panel); standard deviation of the monthly SSS from model and NIOA (a, lower panel); standard deviation of the daily SST from model and TMI (b, upper panel); standard deviation of the daily SSS from model and Aquarius (b, lower panel).

ern part of the domain shows particularly low SST values during June-July-August months.

The seasonal variability of the SSS is shown in Fig. 5. It is clearly evident from the figure that the model very well simulates the SSS seasonal variability. We notice that the AS has higher SSS than BoB in general. The northern BoB has particularly low SSS values during June-July-August (monsoon) and September-October-November (post-monsoon season) as a result of increased freshwater transport from major adjoining rivers (Ganga, Brahmaputra and Irrawaddy) (Sengupta et al., 2006). The southern BoB has higher SSS than northern BoB in all the seasons. We see, however, an exactly opposite nature in the AS. In the southern AS, we find lowest SSS during December-January-February which may be due to coastal runoff, and also due to movement of less saline BoB water towards AS and its mixing with the saltier AS water.

To guage the quality of the model output in simulating the temporal evolution of the SST and SSS, we make an index of these variables in the upper and lower BoB and AS region. The monthly SST and SSS values during 1998–2014 (17 a) are area averaged over the region (7°–11°N, 67°–72°E) in the southern AS (SAS), (16°–20°N, 67°–72°E) in the northern AS (NAS), (87°–92°E, 7°–11°N) in the southern BoB (SBoB), and (16°–20°N, 87°–92°E) in the northern BoB (NBoB). We show in Fig. 6a, the time series of the SST indices for the model as well as TMI. The model and TMI SST time series are highly correlated at values 0.93 and 0.90 in the SAS and NAS, respectively. Similarly, the correlation of 0.94 and 0.96 exists between the model and TMI SST time series in the SBoB and NBoB, respectively. These correlations are significant at 99.9% level. The RMSE between the model and TMI SST time

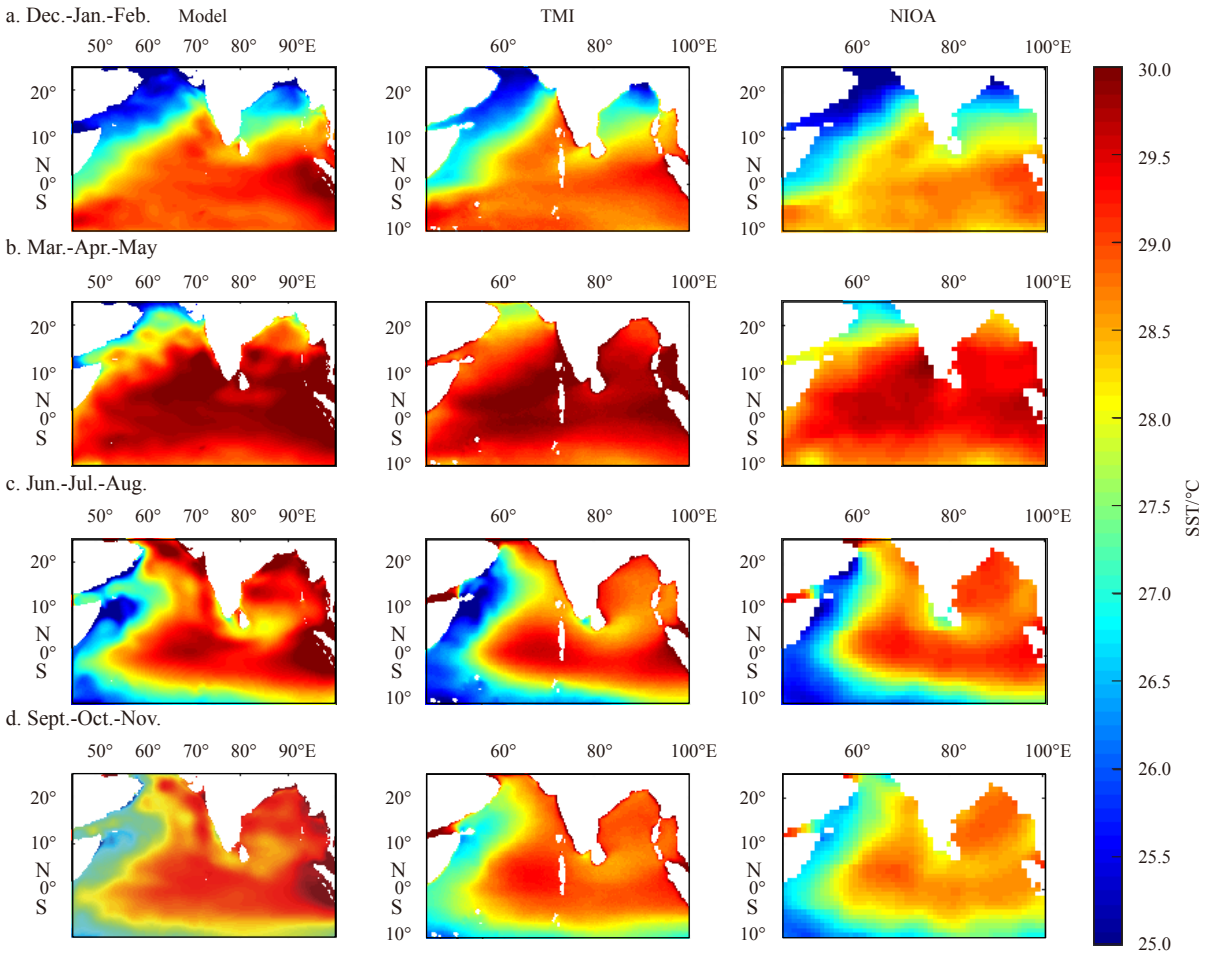

Fig. 4. Seasonal SST map from the model output for December-January-February, March-April-May, June-July-August, and September-October-November during 1998–2014 (first column, top to bottom); seasonal SST map from the corresponding TMI dataset (second column, top to bottom); and seasonal SST map from the corresponding NIOA dataset (third column, top to bottom).

series is 0.33°C (0.55°C) and 0.31°C (0.47°C) in the SAS (NAS) and SBoB (NBoB), respectively. These values are much smaller than the standard deviation of 0.82°C (1.21°C) and 0.87°C (1.51°C) of the TMI SST time series over these regions. The SST time series shows near-periodic (12 months) interannual fluctuations but the trend is nearby absent in all the selected regions over this time period. It is interesting to note that the SST variations in the NAS and NBoB are almost identical to each other, though magnitude is little higher in the BoB. We notice that the range of SST variability is higher in the northern domain (i.e., NAS and NBoB) as compared to southern domain. In the northern domain, the SST peaks during the month of May with a smaller peak occuring in the month of October also. Similarly, the minimum SST is obtained during January–February with another minima occuring during August. In the SAS and SBoB, the SST values are highest during May and lowest during January–February. In the bottom panel of Fig. 6a, we show the SST bias map between the model and TMI values. It may be seen from the figure that the biases are of the same order in all the regions. Morever, barring few exceptions, the biases are generally low. In the years of 2013 and 2014, the March–April SST bias in the NBoB and SBoB, respectively are relatively higher and the model is found to underestimate the SST values. On the other hand, the model overestimates August SST values of 2007 and 2009 in the SAS and NAS regions, respectively.

The monthly time series of the SSS indices in the SAS, NAS, SBoB and NBoB is shown in Fig. 6b for the model and ORAS4 data. The model and ORAS4 monthly SSS time series are significantly correlated with each other in all the regions (Table 3). The RMSE between the two time series is also smaller than the corresponding standard deviations (Table 3). It is seen from the figure that the SSS of the AS is much higher than BoB. The SSS in the SAS remains high with lowest values (~35) observed during March–April. The NAS, on the other hand shows very high SSS values (>36) throughout the year with very small monthly variations. The SBoB SSS values also show small monthly fluctuations around 33. The SSS in the NBoB, however, shows highest monthly variability and ranges between 30 and 34. The lowest SSS values in the NBoB are obtained during the month of October. The model-data bias between the monthly SSS time series of model and ORAS4 is shown in the bottom panel of Fig. 6b. It may be seen from the figure that the SSS bias is very small in all the regions, except in the NBoB. In other words, the model underperforms in the NBoB region, whereas, it performs very well in all other regions in terms of monthly SSS simulation. This may be due to incorrect vertical parametrization and boundary condi-

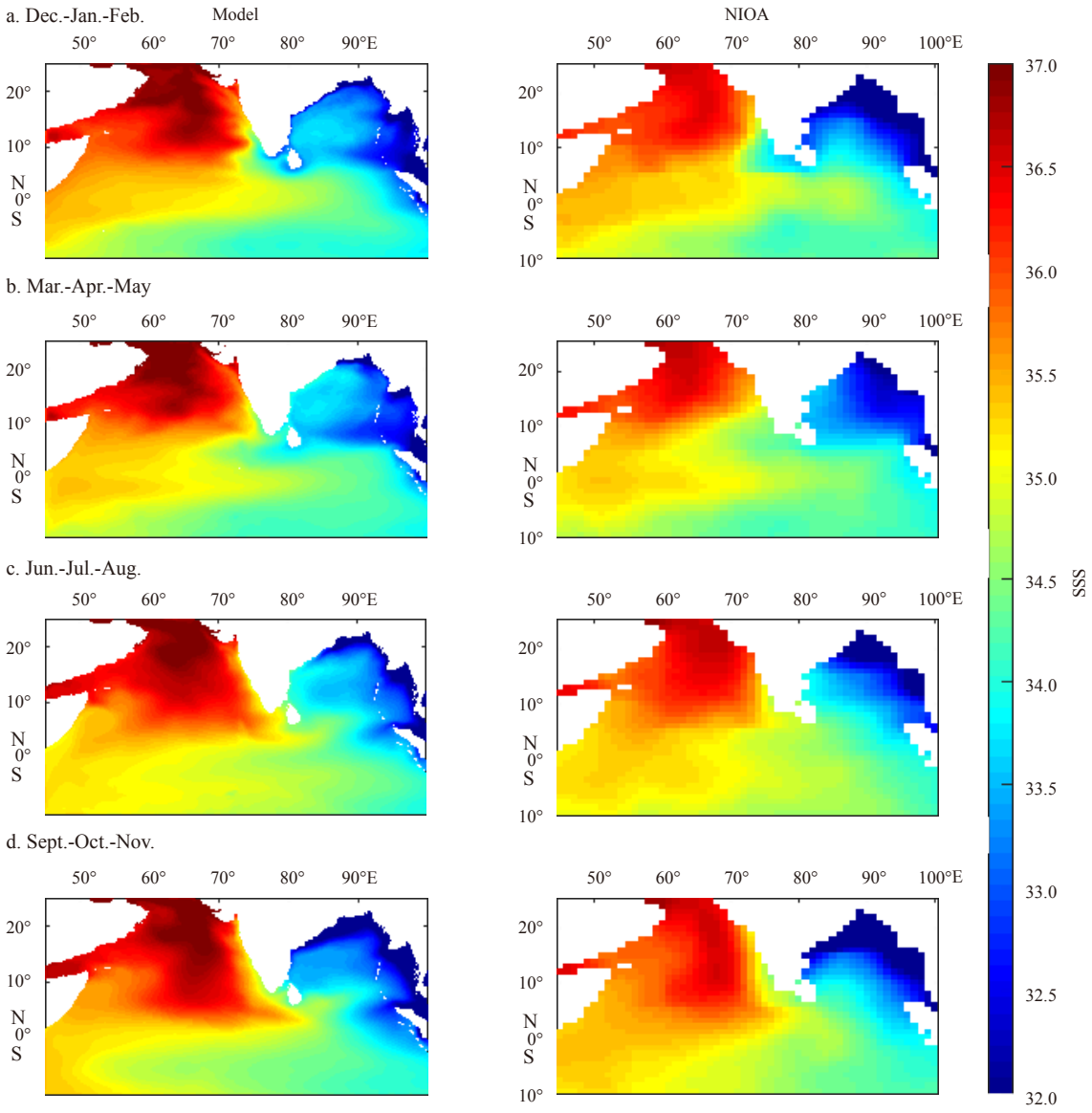

Fig. 5. Seasonal SSS map from the model output for December-January-February, March-April-May, June-July-August, and September-October-November during 1998–2014 (first column, top to bottom); and seasonal SSS map from the corresponding NIOA dataset (second column, top to bottom).

tions in the NBoB. The underperformance of the model's SST and SSS during monsoon (and to some extent post-monsoon) season may also be due to use of very coarse river runoff and precipitation data from the NCEP during these seasons.

It has been argued in recent researches that understanding the intraseaonal variability of the ocean surface variables (more importantly SST) and how it interacts with the atmospheric intraseasonal oscillations is critical for the correct prediction of Indian monsoon rainfall (Schiller and Godfrey, 2003; Li et al., 2015 and references therein; Keerthi et al., 2016). Thus, it will be worthwhile to also study the intraseasonal variability of the SST and SSS over the model domain. For this purpose, we extract the 20–60 d intraseasonal mode from the daily data of model SST area averaged over the NAS, SAS, NBoB and SBoB regions for each season (Fig. 7). The corresponding intraseasonal modes from the TMI observations are also extracted to quantify the model's performance at intraseaonal scale. Table 4 summarizes the correlation and RMSE between the intreaseasonal modes of observation and model. The mean and standard deviation of intraseasonal TMI values are also given in Table 4. The model's ability in simulating the SST variability at intraseasonal scale is clearly evident from Fig. 7 and Table 4. It is clear from the Table that correlation between the model and observation is significantly high and RMSE between the model and observation is less than the standard deviation of observation in all the regions and for the intraseaonal modes of all the seasons. This confirms the realistic simulation of model simulated intreaseaonal modes. Table 4 also shows that the intraseasonal SST of the southern part of AS and BoB (i.e., SAS and SBoB) is in general cooler and more variable as compared to the respective northern parts (i.e., NAS and NBoB). The highest intraseasonal SST variability is seen in the spring season of March-April-May in the SAS (0.64°C) and SBoB (0.61°C). On the other hand, the lowest intraseasonal SST variability is obtained in winter months of December-January-

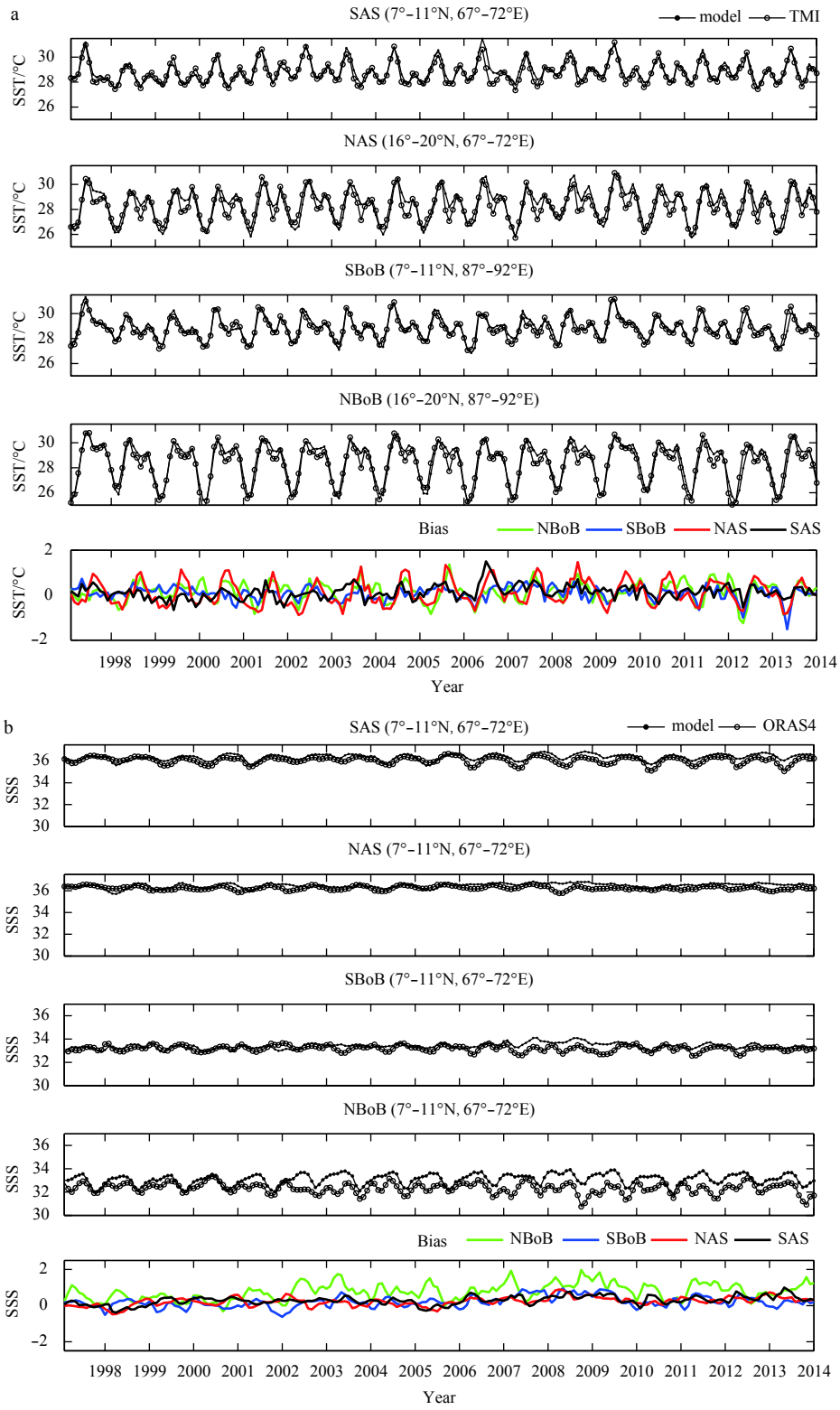

Fig. 6. Quality of model's SST and SSS in northern and southern part of AS and BoB. a. Monthly time series of the SST from model and TMI dataset during 1998–2014. The SST from the model and TMI is shown by dot and circle, respectively. The model-observation bias is shown in fifth row. b. Monthly time series of the SSS from model and ORAS4 dataset during 1998–2014. The SSS from the model and ORAS4 is shown by dot and circle, respectively. The model-observation bias is shown in fifth row.

February in the NAS (0.30°C) and NBoB (0.28°C) regions. The intraseasonal variability of the SSS over the model domain is not given since the continuous daily SSS observations for the period of simulation are not available.

To demonstrate the quality of model simulation in representing the sub-surface characteristics of temperature and salinity,

Table 3. SST and SSS monthly variability over the NAS, SAS, NBoB and SBoB regions of model domain

Variable	Regions											
	NAS			SAS			NBoB			SBoB		
	RMSE	$\mu \pm \sigma$	r	RMSE	$\mu \pm \sigma$	r	RMSE	$\mu \pm \sigma$	r	RMSE	$\mu \pm \sigma$	r
SST	0.55	28.3 ± 1.21	0.90	0.33	28.7 ± 0.82	0.93	0.47	28.3 ± 1.51	0.96	0.31	28.8 ± 0.87	0.94
SSS	0.12	36.25 ± 0.18	0.64	0.24	36.0 ± 0.33	0.81	0.39	32.3 ± 0.46	0.72	0.17	33.19 ± 0.25	0.60

Note: RMSE is the root mean square error between model and observation, μ and σ are mean and standard deviation of observation, respectively, and r represents correlation coefficient between model and observation.

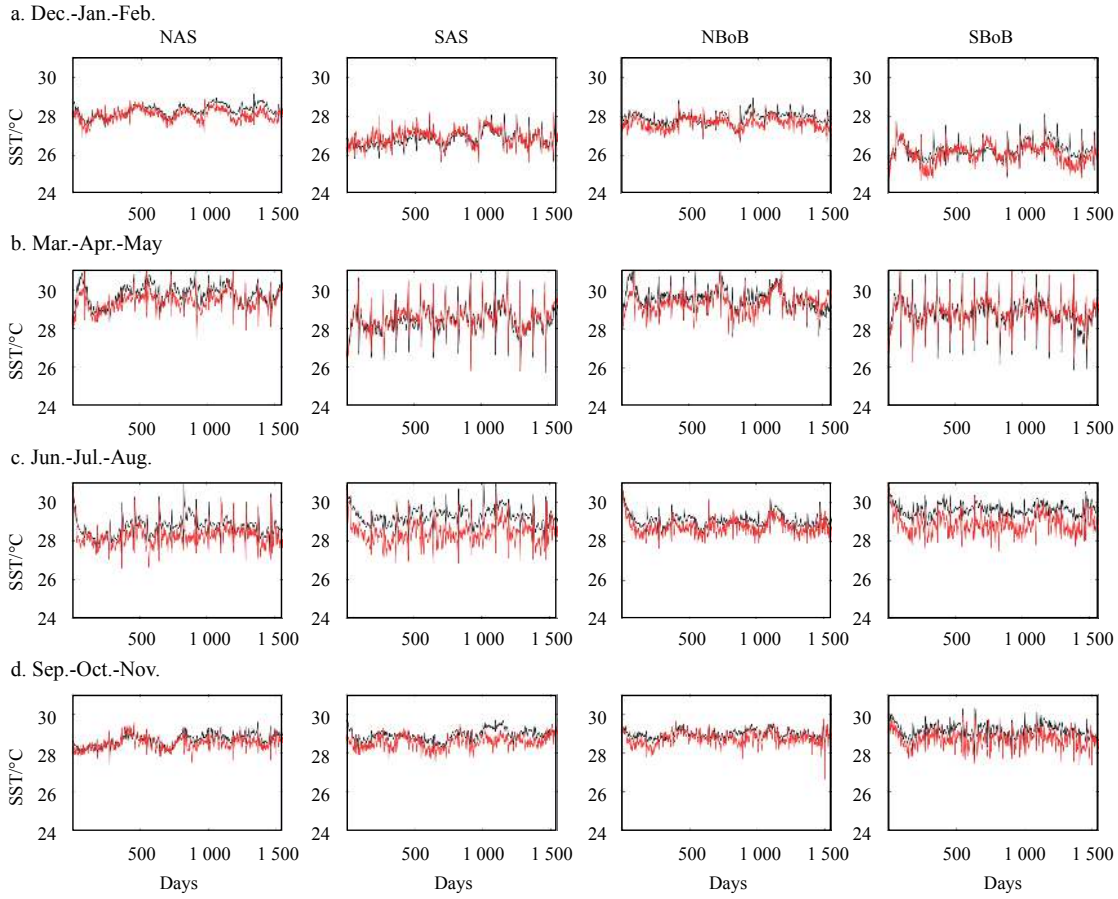

Fig. 7. 20–60 d intraseasonal SST time series from model (black) and TMI dataset (red) during 1998–2014 area averaged over the NAS, SAS, NBoB and SBoB regions.

Table 4. The 20–60 d intraseasonal SST variability over the NAS, SAS, NBoB and SBoB regions of model domain

Seasons	Regions											
	NAS			SAS			NBoB			SBoB		
	RMSE	$\mu \pm \sigma$	r	RMSE	$\mu \pm \sigma$	r	RMSE	$\mu \pm \sigma$	r	RMSE	$\mu \pm \sigma$	r
Dec.-Jan.-Feb.	0.22	28.0 ± 0.30	0.78	0.28	26.9 ± 0.40	0.78	0.24	27.6 ± 0.28	0.66	0.29	26.0 ± 0.47	0.74
Mar.-Apr.-May	0.38	29.4 ± 0.48	0.82	0.31	28.5 ± 0.64	0.91	0.36	29.3 ± 0.49	0.72	0.36	28.8 ± 0.61	0.88
Jun.-Jul.-Aug.	0.46	28.2 ± 0.51	0.81	0.50	28.4 ± 0.56	0.86	0.30	28.7 ± 0.38	0.83	0.40	28.9 ± 0.48	0.82
Sep.-Oct.-Nov.	0.18	28.5 ± 0.32	0.71	0.26	28.6 ± 0.32	0.64	0.23	28.7 ± 0.32	0.68	0.35	28.7 ± 0.41	0.73

Note: RMSE is the root mean square error between model and TMI observation, μ and σ are mean and standard deviation of observation, respectively and r represents correlation coefficient between model and TMI observation.

we show in Fig. 8, the latitude-depth maps of temperature and salinity at 70°E in the AS and 90°E in the BoB. The model caputures the layered structured of the upper ocean with correct magnitude very well. One of the possible regions for the small discrepencies, if any, in the mixed layer depth and thermocline observed between model and NIOA may be their different horizonal and vertical resolutions. The sub-surface temperature and salinity strucutures are very different in the AS and BoB. The latit-

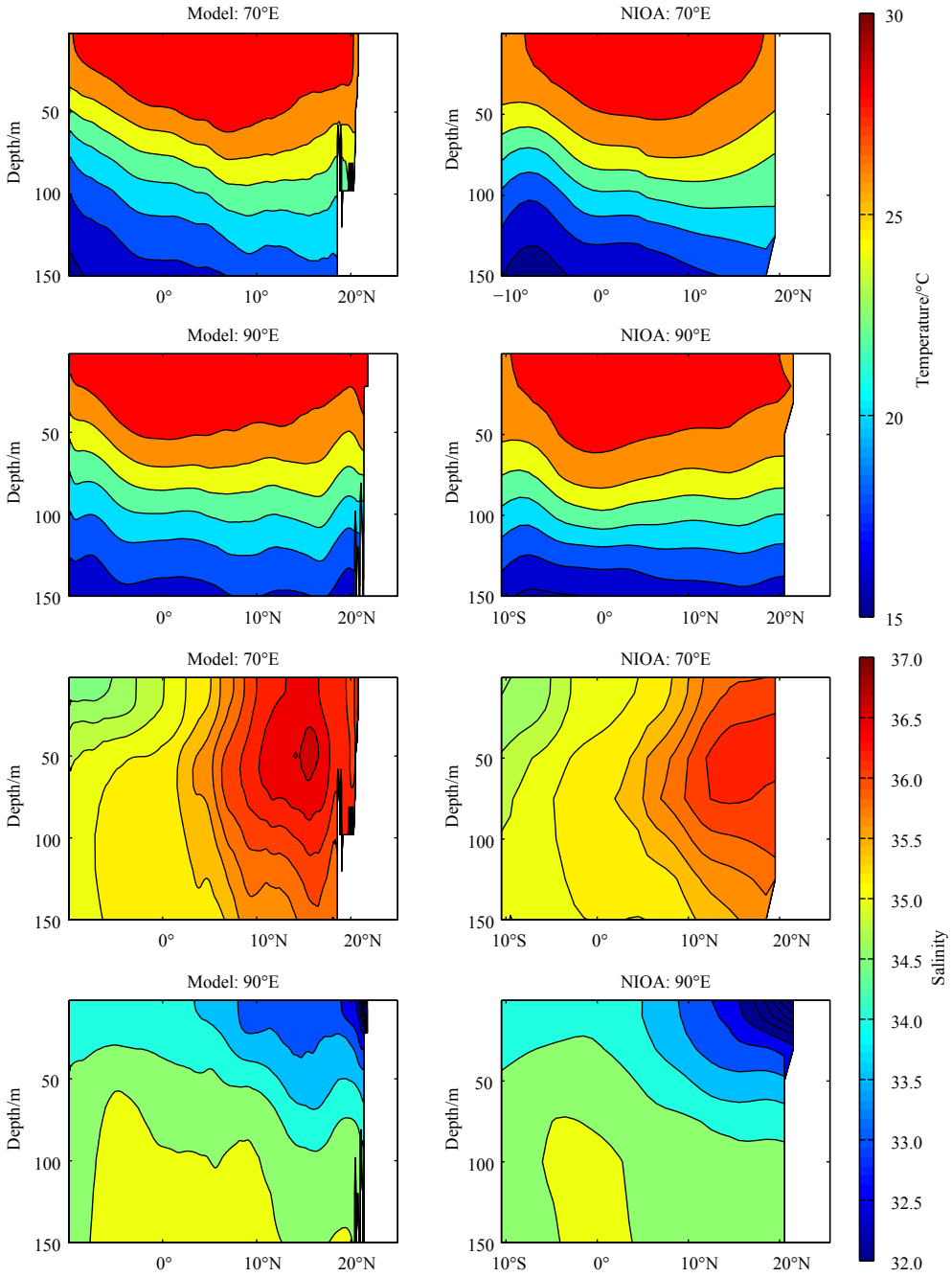

Fig. 8. Latitude-depth map of temperature and salinity. The model temperature and salinity values shown in the first column are compared with the corresponding NIOA values shown in the second column.

ude-depth map of the temperature shows that the thermocline in the AS has a tilted structure with values increasing from south to north. The BoB, however, shows no such nature and thermocline is nearly flat. The salinity diagram shows that the values are nearly opposite in the AS and BoB at higher latitudes. For example, in the region 15°–22°N, where the highest salinity values are observed in the AS, the BoB region shows the lowest salinity. The low salinity of the BoB in this region is mainly attributed to freshening of water as a result of river runoff from major adjoining rivers of the region. On the other hand, higher evaporation than precipitation in the northern AS is the principal reason of high salinity in that region. The presence of salty outflow from the Red Sea and Persian Gulf is also the reason for high salinity of the region.

3.2 *Mixed layer depth*

The estimation of mixed layer depth (MLD) is very important for oceanic investigations including upper ocean productivity, air-sea exchange processes, and long-term climate change (Thomson and Fine, 2003, Keerthi et al., 2013). We compute the MLD of the model domain using Lorbacher et al. (2006) criterion, which is based on the shallowest extreme curvature of near surface density profiles. We show in Fig. 9 (upper panel) the spatial maps of the seasonal variation of the MLD over our region of study. The corresponding MLD maps from ARGO (Holte et al., 2016) are also shown in Fig. 9 (lower panel) for comparison.

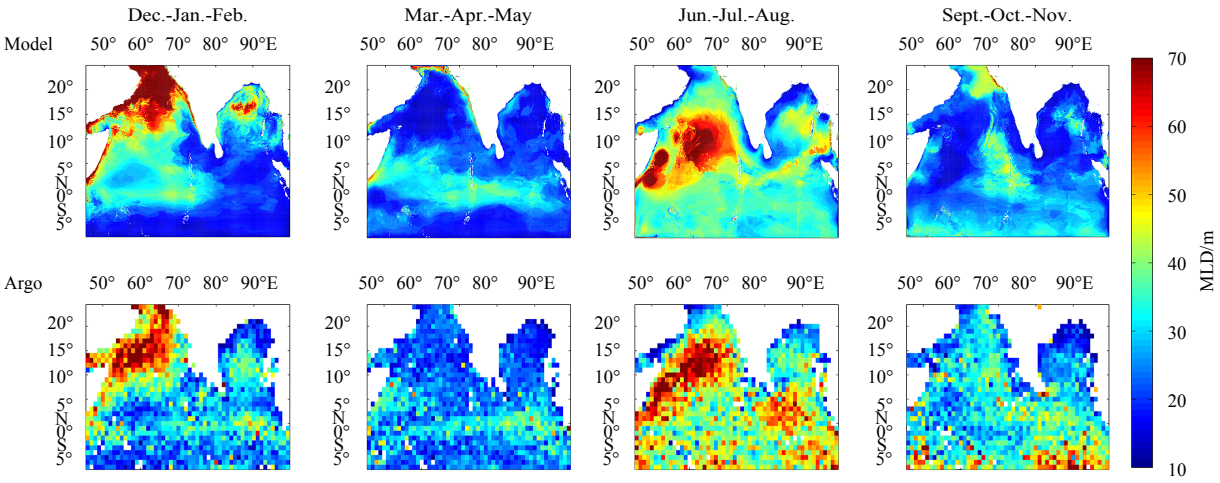

Fig. 9. Seasonal mixed layer depth (MLD) variability from model (upper panel); and from Argo (lower panel).

Holte et al. (2016) computed MLD using more than 1 250 000 Argo profiles (collected between January 2000 and May 2016) and a hybrid algorithm (Holte and Talley, 2009).

Figure 9 clearly demonstrates the model's ability in correct estimation of the MLD seasonal variations (both spatially as well as temporally). The model MLD values are close to the ARGO MLD estimates in all the seasons. Moreover, our results also suggest that the MLD is deeper in the AS as compared to the BoB (de Boyer Montégut et al., 2007, Keerthi et al., 2013). The MLD remains low in the upper northern BoB in all the seasons. The lowest MLD values are observed in the months of March-April-May and highest during December-January-February. The mean MLD in the AS region during December-January-February, March-April-May, June-July-August and September-October-November is 50, 22, 44, 27 m, respectively. On the other hand, the mean MLD in the BoB region during the same season is 31, 18, 32, 23 m, respectively. Thus, the mean MLD of the AS remains higher as compared to the BoB during all the seasons. The mean MLD during March-April-May is very shallow in the AS as well as BoB. We, however, observe intermediate MLD values during monsoon season of June-July-August. Interestingly, in the post-monsoon months of September-October-November, the mean MLD of the AS and BoB remain very close to each other. The maximum MLD is obtained during winter (December-January-February) with AS and BoB having MLD values of 150 m and 67 m, respectively. The minimum MLD in the AS and BoB (nearly 11–12 m) is, however, obtained during the spring (March-April-May). It is also interesting to note that the AS and BoB MLD during December-January-February and June-July-August exhibits dipole like structure with opposite signs during these seasons. For example, during the December-January-February, the northern and central AS and BoB show high MLD whereas southern part of domain shows low MLD values. Contrary to this, we observe higher values of MLD in southern domain as compared to northern and central AS and BoB during June-July-August.

Figure 9 shows that the season-to-season variability of the MLD is quite significant. In general, the air-sea fluxes are considered as drivers of the MLD variability. It is, therefore, important to illustrate and understand the seasonal MLD variability vis-à-vis seasonal changes in the air-sea fluxes. For this purpose, we show in Fig. 10a the seasonal map of air-sea fluxes, namely, wind stress, net heat flux, and net freshwater flux (buoyancy flux). It is clear from the 1st column of Fig. 10a that the negative buoyancy flux brought by the excess of evaporation over precipitation largely explains the relatively deep MLDs in December-January-February season (de Boyer Montégut et al., 2007) seen in Fig. 9 (the 1st column). In addition to this, low shortwave radiation flux and high negative latent heat flux and sensible heat flux (Fig. 10b, the 1st column) (resulting in negative net heat flux) is also responsible for deep MLDs during December-January-February. Whereas, the main reason behind very low MLD values in the AS and BoB during March-April-May are very weak easterlies (weak wind stress, the 2nd column of Fig. 10a) over the region of interest. Very high shortwave radiation flux (Fig. 10b, the 2nd column) (resulting in positive net heat flux) also contributes to MLD shallowing during March-April-May. During the monsoon (June-July-August) season (Fig. 10a, the 3rd column), high wind stress and low shortwave radiation as well as high negative latent heat flux (Fig. 10b, the 3rd column) (resulting in negative net heat flux) are responsible for high MLD values in the southern AS. On the other hand, due to high freshwater flux (precipitation-evaporation) in the northern BoB, the MLD remain shallower. In the post-monsoon months of September-October-November, the MLDs, along coastal and adjoining areas in the BoB have low (to very low) values, whereas other regions of the domain also have low to intermediate values. This happens as a result of low wind stress in the region of interest (Fig. 10a, the 4th column) and increased freshwater flux (runoff from rivers) in the BoB. The net heat flux in most parts of the AS and BoB remains very small due to cancelling effect of its component fluxes (Fig. 10b; the 4th column).

3.3 *Mixed layer heat budget*

In order to understand the seasonal variability of the mixed layer temperature in general, and SST in particular, the estimation of mixed layer heat budget is important. Even though it is largely believed that the major contribution in the SST variability comes from seasonally varying air-sea fluxes, however, the horizontal and vertical temperature advections also play a major role at some locations. It will be, therefore, useful to explicitly compute all possible contributions to the mixed layer heat budget. This will help us understand and quantify importance of each individual term in the spatio-temporal variability of SST.

Following Stevenson and Niiler (1983), Moisan and Niiler (1998), and Huang et al. (2010), we compute the mixed layer heat

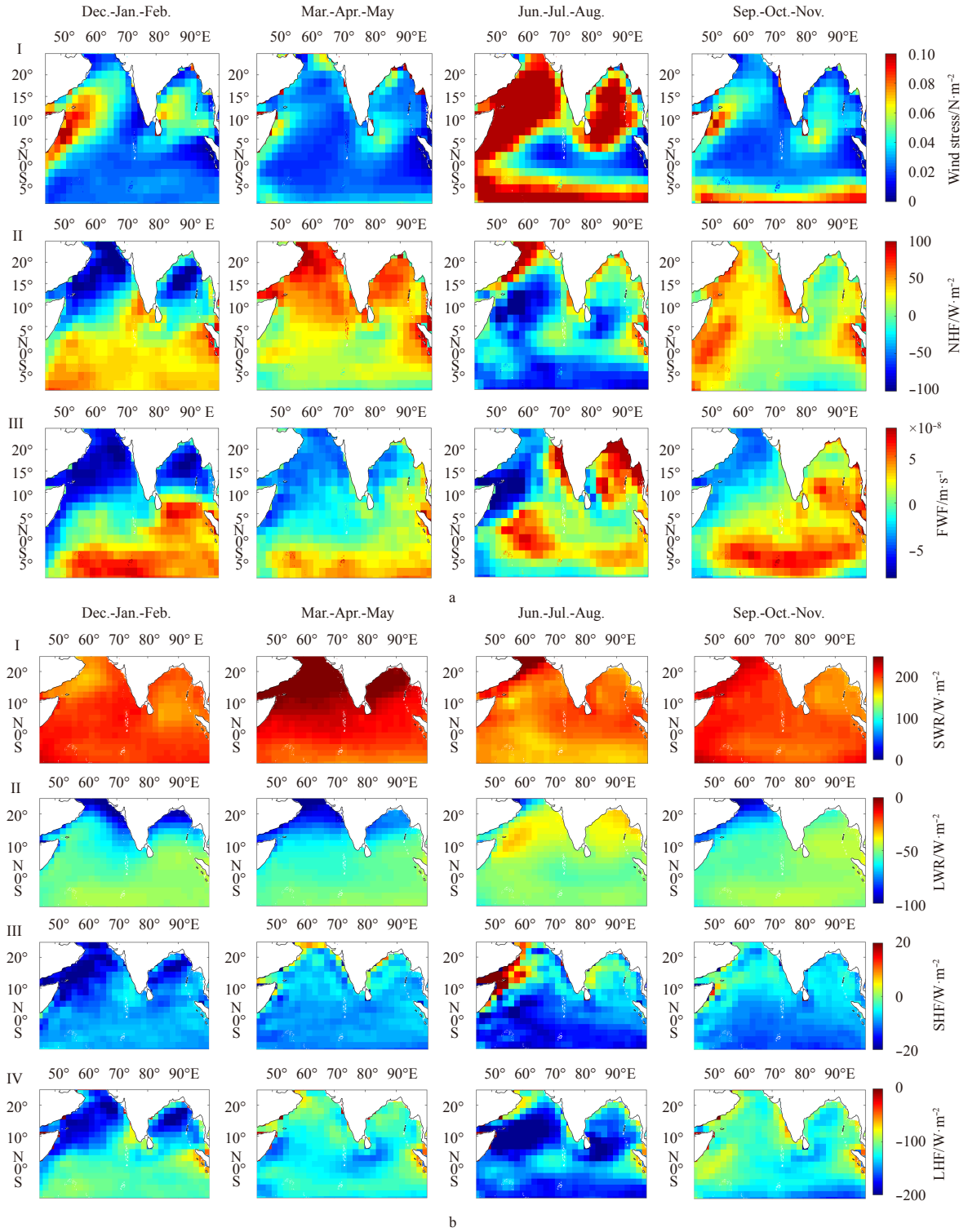

Fig. 10. Seasonal map of wind stress, net heat flux (NHF) and net freshwater flux (FWF) (a); and seasonal map of shortwave radiation flux (SWR), downward longwave radiation flux (LWR), sensible heat flux (SHF) and latent heat flux (LHF) (b).

budget as

$$T_t = F, \tag{1}$$

where $T_t \left(= \frac{\partial T}{\partial t}\right)$ is the mixed layer temperature tendency and F is the forcing. The forcing is sum of zonal advection (Q_u), meridional advection (Q_v), vertical entrainment (Q_w), net surface heat flux (Q_q), and vertical diffusion (Q_{zz}). In other words, F is expressed as

$$F = Q_u + Q_v + Q_w + Q_q + Q_{zz}. \tag{2}$$

The consistency between T_t and F is used to check the clos-

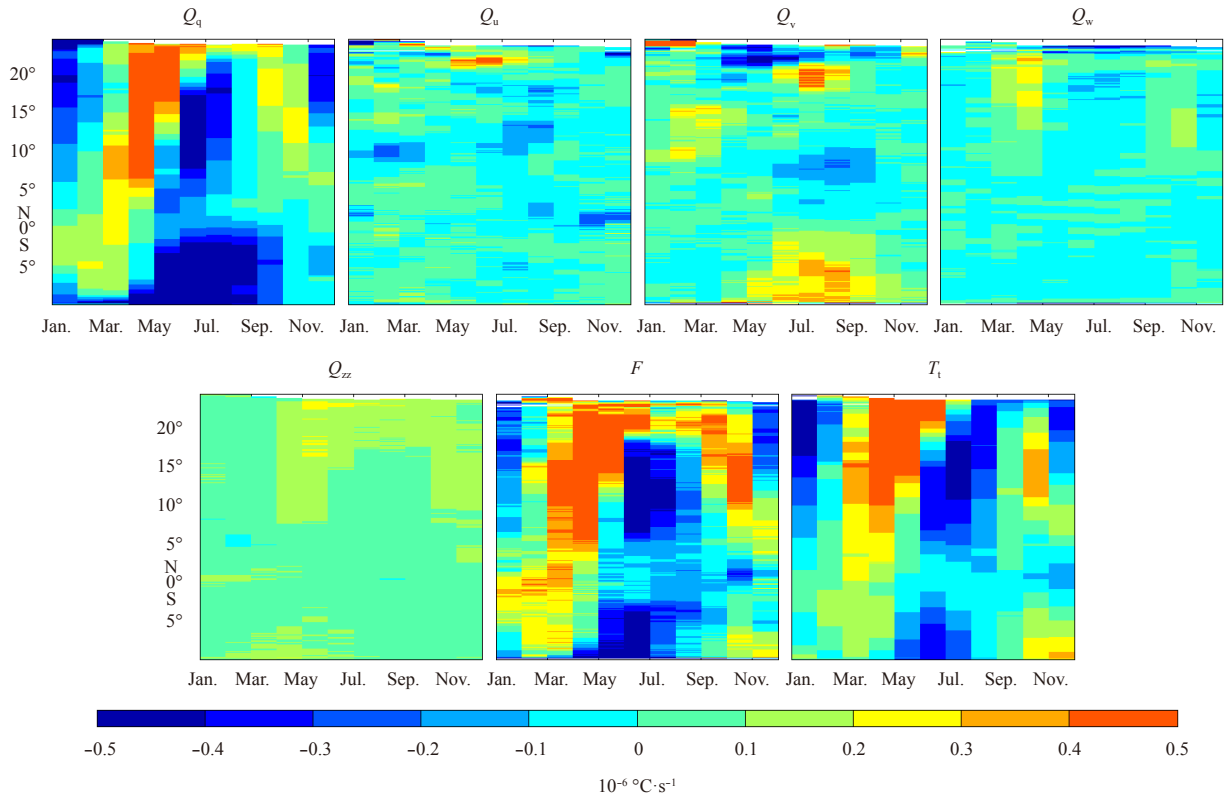

Fig. 11. Time-latitude map of mixed layer heat budget at 67°E.

ure of the temperature equation. For further computational details on each of these terms please refer to Appendix A of Huang et al. (2010).

The time-latitude map of different terms of mixed layer heat budget at 67°E is shown in Fig. 11. We see from figure that even though T_t and F are very close to each other (thus giving good closure of temperature tendency), however, they are not exactly the same. The difference between them may be due to missing contributions from (weak horizontal) diffusion term. The differences could also be due to numerical errors. It is clear from the figure that out of all forcing terms, Q_q is most dominant term. The contribution from zonal advection Q_u is generally insignificant except few places. The meridional advection Q_v on the other hand helps in increasing the mixed layer heat budget (and SST) of southern part of domain (south of 5°S) during July to September. The Q_v reduces mixed layer heat budget between 5° and 10°N during June to October and north of 21°N during April to November. The vertical entrainment Q_w remains very low in the AS except during April. The diffusion term Q_{zz} although remains low, but helps in increasing the mixed layer heat budget north of 15°N during April to November. The contributions from Q_q (and therefore forcing F) suggest that in the Arabian Sea at 67°E (north of 5°N), we get low SST in December–February, high SST in March–May, low SST again in June–August, and intermediate SST values in September–November months. This is consistent with the SST variability (at 67°E) shown in Fig. 4. The F and Q_q values of Fig. 11 also suggest that the SST of the southern part of domain remains low during May–September months of the year.

The time-latitude map of mixed layer heat budget at 90°E is shown in Fig. 12. In this case also, we clearly notice that the largest contribution to the mixed layer heat budget is coming from air-sea fluxes Q_q. While the effect of vertical entrainment Q_w is smaller in this case compared to at 67°E, however, the spatio-temporal contributions from zonal advection Q_u are larger here especially during summer monsoon months (June–September) between 5°–10°N. The meridional advection Q_v plays a similar role in this case as seen at 67°E. In the southern part of domain it tends to increase the SST during May–September. On the other hand, negative Q_v values in northern part of domain (between 0–10°N) during Jun–October helps in maintaining intermediate SST values in these regions during these months. The vertical entrainment and diffusion terms give only small positive contribution (north of 15°N) in F at 90°E. The Q_q (and F) map clearly suggests that at 90°E in the Bay of Bengal (north of 5°N), the SST tendency should remain low during December–January and high during March–April. The SST tendency also remains low at 90°E between 5°–12°N and south of 5°S during May–September. These observations are also consistent with the SST variability shown in Fig. 4 thus demonstrating the robustness of mixed layer heat budget calculations.

For correctly capturing the mechanisms responsible for mixed layer temperature (or SST) variability using mixed layer heat budget analysis, it is important to see if a reasonable closure of heat budget exists using the model output. To demonstrate the closure, we show the seasonal variability of forcing F and mixed layer temperature tendency T_t in Fig. 13. The bias map (bottom panel of Fig. 13) suggests that the mixed layer temperature budgets have a good closure, indicating that the results regarding the mechanisms controlling the mixed layer temperature (or SST) evolution are quite robust. The differences between them point towards the role of missing term of horizontal diffusion processes and numerical errors in our calculations. Nevertheless, the variation of seasonal variability of F and T_t is largely coherent with the seasonal evolution of SST seen in Fig. 4.

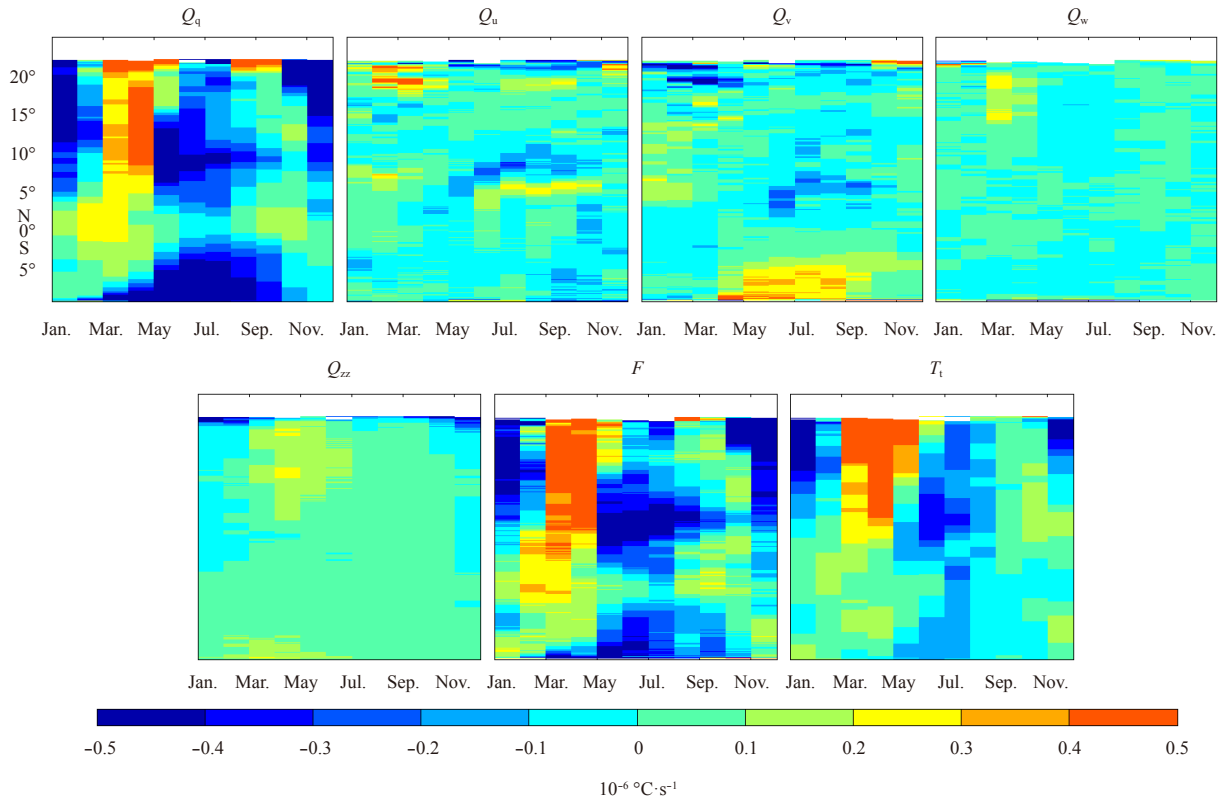

Fig. 12. Time-latitude map of mixed layer heat budget at 90°E.

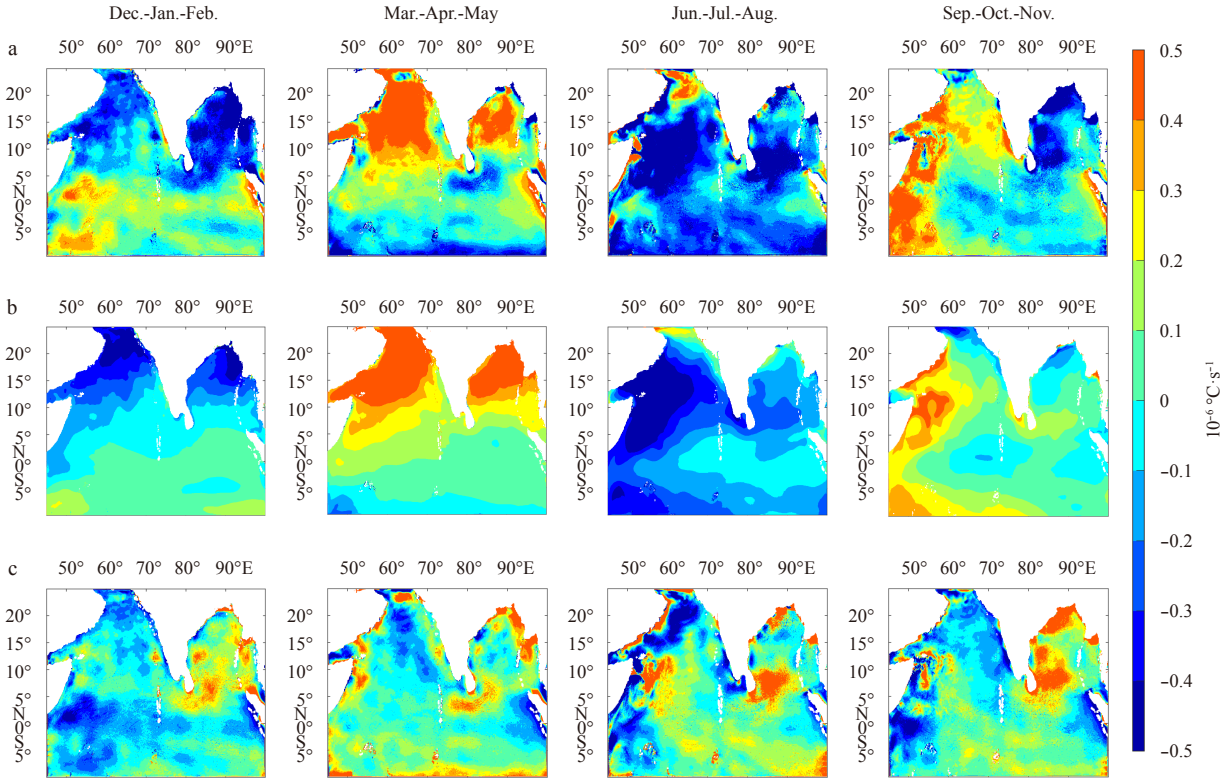

Fig. 13. Seasonal variability of forcing F (a); mixed layer temperature tendency T_t (b). c shows the bias map between F and T_t.

The monthly mixed layer heat budget area-averaged over the SAS, NAS, SBoB and NBoB region is shown in Fig. 14. In the SAS region, the highest positive (negative) heat budget is obtained during April (June). We notice that F and T_t values are close to each other. Apart from Q_q, the contribution from all other terms is small. In the NAS region, the highest positive (negative) heat

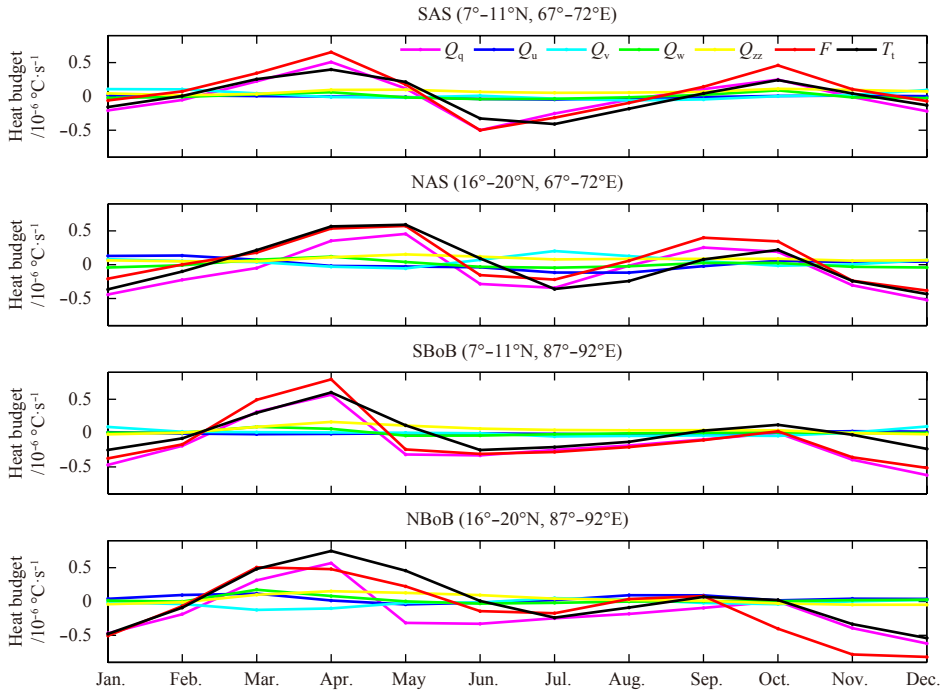

Fig. 14. Monthly mixed layer heat budget averaged over the SAS, NAS, SBoB and NBoB regions.

budget is obtained during May (July). We notice that F and T_t values are close to each other except during June–September. In addition to Q_q, the contribution from vertical advection Q_v and diffusion Q_{zz} also becomes important in these months. These terms try to increase the mixed layer heat so that good closure between F and T_t may be obtained. In the SBoB, the highest positive (negative) heat budget is obtained during April (December–January). We see a good closure between F and T_t except during May and November–December. The maximum (minimum) contribution to the mixed layer heat budget comes from air-sea fluxes (horizontal entrainment). In the NBoB, the highest positive (negative) heat budget is obtained during April (November–December). The F and T_t are close to each other in all the months, except during October-December. In the NBoB, we see significant contribution in the mixed layer heat budget coming from Q_v and Q_{zz}, although with opposite signs (especially during February–June) with maximum contribution still coming from Q_q. While the meridional advection reduces the mixed layer heat budget of the region, the vertical diffusion tends to increase it. It is clear from the Figure, that the net air-sea heat flux plays most important role in controlling the mixed layer temperature variability of the northern Indian Ocean.

3.4 *Surface currents and volume transport*

In an effort to demonstrate the quality of model solutions in simulating the surface circulation, we show in Fig. 15 the seasonally varying surface currents of the region during the period of simulation. The model results are compared with the OSCAR surface current (Bonjean and Lagerloef, 2002) data, which is a combination of *in situ* and satellite altimeter derived current products. We find that the model surface currents match very well with OSCAR. We notice from Fig. 15 that during December-January-February (winter monsoon season), the southeasterly currents flow northwards in the southern AS and BoB. In the AS, the flow is dominantly meridional (south-north), whereas upper BoB shows a weak anti-cyclonic behavior. During March-April-May strong anticyclonic motion is observed in the BoB covering the northern and parts of central bay. The poleward East Indian coastal current (EICC) (Schott and McCreary, 2001) is also seen in the upper bay. The currents, on the other hand, are found to be weak in the AS. In the summer monsoon season of June-July-August, the BoB currents are dominantly (zonal) eastwards, except in the northernmost bay, where we notice a feeble cyclonic circulation. The model perfectly reproduces the direction of the observed currents although with somewhat greater magnitudes (Fig. 15; the 3rd column). In the AS, we notice northwesterly currents (including West Indian coastal current, WICC) flowing southwards which are almost opposite in direction to December-January-February currents. During September-October-November, we observe cyclonic circulation in the northern bay. Both the EICC and WICC flow equatorwards. The zonal summer monsoon current (SMC) flowing from southern AS towards southern BoB during June-July-August and winter monsoon current (WMC) flowing in exactly opposite direction during December-January-February are also well reproduced by the model. The discrepancies in modeled and observed (OSCAR) surface current data seen in the 3rd column of Fig. 15 may be mainly due to their very different horizontal and temporal resolutions. For example, the OSCAR data is available at 1/3-degree horizontal resolution and 5 d of temporal resolution. On the other hand, our model output uses daily data at a horizontal resolution of 0.09 degree.

We also compute zonal and meridional volume transport across different sections (shown in Fig. 1 by vertical and horizontal lines, respectively) in the AS and BoB using Eq. (3) as below:

$$\text{zonal volume transport} = \int_0^{L_y}\int_{-h}^{0} u\,(x,y,z,t)\,\mathrm{d}z\mathrm{d}y, \qquad (3a)$$

$$\text{meridional volume transport} = \int_0^{L_x}\int_{-h}^{0} v\,(x,y,z,t)\,\mathrm{d}z\mathrm{d}x, \qquad (3b)$$

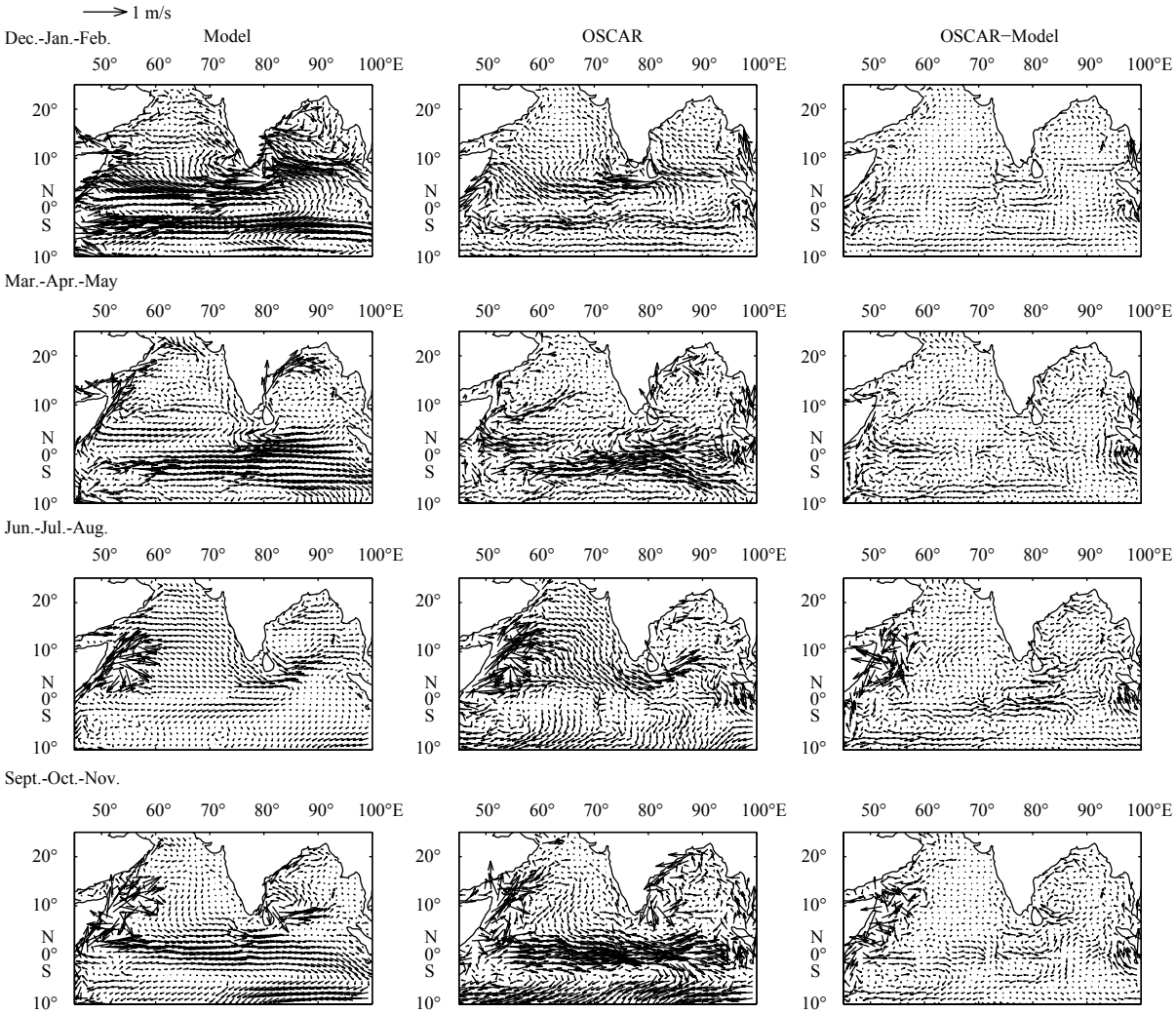

Fig. 15. Seasonal variability of surface currents during 1998–2014 from model data, OSCAR observations and difference between OSCAR and model data.

where h is the ocean depth at position (x, y), u is the zonal velocity, v is the meridional velocity, Ly and Lx are the widths of the meridional and zonal transects, respectively. The meridional volume transport for the upper 100 m is computed along the section (12°N, 71°–75°E) in the Arabian sea and (12°N, 80°–84°E) in the Bay of Bengal. The zonal transport for the upper 100 m is computed along the section (4°–7°N, 76°E) at the interface of AS and BoB. These sections are so chosen that by studying the transport of water mass across them (which includes surface as well as intermediate and deep ocean), we can infer the variability of the monsoonal currents, namely, WICC in AS, EICC in the BoB, and SMC (WMC) at the interface of AS and BoB on seasonal and interannual time scales. Moreover, this will also help us quantify seasonal transport of water mass from the BoB to AS and vice versa during summer and winter monsoon seasons. In Fig. 16, we show the monthly climatology of the volume transport across these sections and compare the results with the corresponding values from the ECCO state estimates. Figure 16 (upper panel) shows that in the AS section, the peak north to south meridional transport (–2.4×10^6 m^3/s) is found during July (monsoon season), whereas peak south to north transport (+3.7×10^6 m^3/s) is obtained during November-December (post-monsoon season). However, the annually averaged volume transport across this section is very small ((0.1± 1.06)×10^6 m^3/s). Similarly, in the BoB (Fig. 16, middle panel) the mean meridional transport across the chosen section is nearly zero (–0.02±2.2)×10^6 m^3/s, i.e., almost equal amount of water flows through these section in the north to south and south to north directions. The peak north-to-south meridional volume transport (–2.6×10^6 m^3/s) across the BoB section is seen during February-March, whereas highest south to north transport is obtained during monsoon season of October-November (+2.7×10^6 m^3/s). Thus, the signs of meridional volume transport in the AS and BoB are almost opposite to each other (r = –0.75) during different months of the year. However, the difference between the AS and the BoB meridional volume transport should not be simply looked as opposite in phase, because the transport of EICC has a semiannual component, whereas the WICC has a single peak and trough over a year. The correlation between volume transport time series obtained from the model and ECCO state estimate is 0.81 and 0.85 in the AS and BoB, respectively. Even though these correlations are highly significant, however, phase differences between the model and ECCO values are seen in the BoB during some months. The zonal volume transport across a section at the interface of AS and BoB is shown

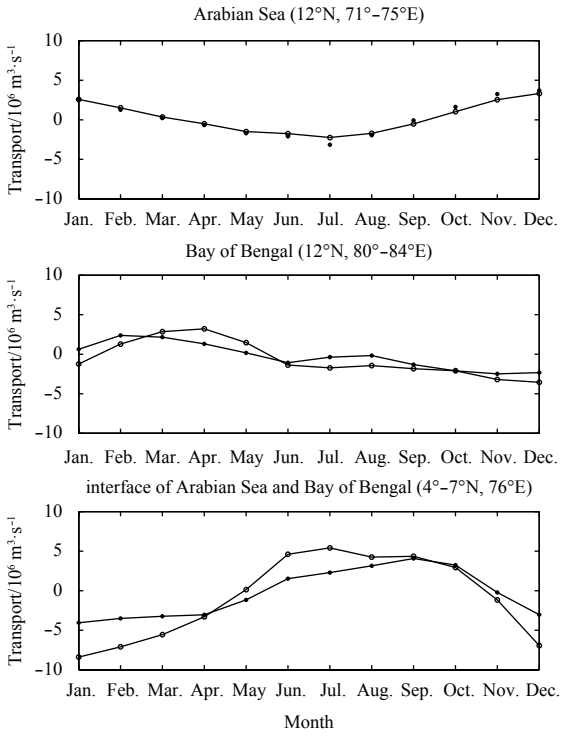

Fig. 16. Seasonal variability of the meridional volume transport computed across the section (12°N, 71°–75°E) in the Arabian Sea (upper panel); meridional volume transport computed across the section (12°N, 80°–84°E) in the Bay of Bengal (middle panel); and zonal volume transport computed across the section (4°–7°N, 76°E) at the interface of Arabian Sea and Bay of Bengal (lower panel). The values from the model and ECCO2 are shown by star and circle, respectively.

in Fig. 16 (lower panel). It is clear from the Figure that the peak east-west transport (–4.1×10^6 m^3/s) is obtained during January (winter season), whereas the peak zonal transport (+4.5×10^6 m^3/s) in opposite direction i.e., west-east direction is observed during August–September (summer monsoon) months. The correlation between model and ECCO derived zonal transport time series is 0.95. The mean zonal flow across this section is from east to west (i.e., from BoB to AS) with transport in the range of (–0.6± 2.2)×10^6 m^3/s.

4 Conclusions

An ocean circulation model, MITgcm is configured to run at a horizontal resolution of 10 km in the northern Indian Ocean around (10°S–25°N, 45°–100°E) covering both the Arabian Sea as well as Bay of Bengal. It is shown that the regional high-resolution ocean circulation model realistically simulates the circulation and hydrography of the Arabian Sea and Bay of Bengal during 1998–2014. For example, the seasonal variability of the surface as well as sub-surface temperature and salinity compares well with the best available observations. The temporal evolution of the SST and SSS is studied in terms area-averaged indices of these variables in the upper and lower BoB and AS regions. The mixed layer depth of the region is computed and its spatio-temporal variability is studied for the period of simulation. The lowest MLD values are observed during spring (March-April-May) months and highest during winter (December-January-February). We use surface air-sea fluxes to explain seasonal mixed layer depth variability. The mixed layer heat budget analysis is carried out to understand factors responsible for the seasonal evolution of mixed layer temperature (SST). The contributions from seasonally varying air-sea fluxes, horizontal temperature advection, vertical entrainment and diffusion are taken into account for this purpose. The results show that surface fluxes play a dominant role on the SST variability. The zonal and meridional volume transport across different sections in the Arabian Sea and Bay of Bengal are also computed and characteristics of monsoonal currents are examined in the light of these. The signs of meridional volume transport in the Arabian Sea and Bay of Bengal are almost opposite to each other. In the present study we are able to demonstrate the quality of our high-resolution hydrography, mixed layer depth, and velocity estimates over the northern Indian Ocean. Our future work will focus on reducing the model-observation misfits using data assimilation.

Acknowledgements

Alok Kumar Mishra and Atul Srivastava are thankful to ISRO and MoES for providing junior research fellowship. Suneet Dwivedi is thankful to MoES/ISRO/DST, Govt. of India for financial assistance in the form of research projects. Thanks are also due to NIO, NCEP, ECCO, and ORAS4 communities for providing their datasets freely available. TMI data are produced by remote sensing systems and sponsored by the NASA earth sciences program. Data are available at www.remss.com.

References

Achuthavarier D, Krishnamurthy V, Kirtman B P, et al. 2012. Role of the Indian Ocean in the ENSO-Indian summer monsoon teleconnection in the NCEP climate forecast system. Journal of Climate, 25(7): 2490–2508, doi: 10.1175/JCLI-D-11-00111.1

Agarwal N, Sharma R, Basu S K, et al. 2007. Evaluation of relative performance of QuikSCAT and NCEP re-analysis winds through simulations by an OGCM. Deep Sea Research Part I: Oceanographic Research Papers, 54(8): 1311–1328, doi: 10.1016/j.dsr.2007.04.006

Akhil V P, Durand F, Lengaigne M, et al. 2014. A modeling study of the processes of surface salinity seasonal cycle in the Bay of Bengal. Journal of Geophysical Research: Oceans, 119(6): 3926–3947, doi: 10.1002/2013JC009632

Ali M M, Nagamani P V, Sharma N, et al. 2015. Relationship between ocean mean temperatures and Indian summer monsoon rainfall. Atmospheric Science Letters, 16(3): 408–413, doi: 10.1002/asl2.576

Annamalai H, Murtugudde R. 2004. Role of the Indian Ocean in regional climate variability. In: Wang C, Xie S P, CartonJ A, eds. Earth's Climate: The Ocean-Atmosphere Interaction. Washington, DC: AGU, 213-246

Annamalai H, Xie S P, McCreary J P, et al. 2005. Impact of Indian Ocean sea surface temperature on developing El Niño. Journal of Climate, 18(2): 302–319, doi: 10.1175/JCLI-3268.1

Balmaseda M A, Mogensen K, Weaver A T. 2013. Evaluation of the ECMWF ocean reanalysis system ORAS4. Quarterly Journal of the Royal Meteorological Society, 139(674): 1132–1161, doi: 10.1002/qj.v139.674

Bates N R, Pequignet A C, Sabine C L. 2006a. Ocean carbon cycling in the Indian Ocean: 1. Spatiotemporal variability of inorganic carbon and air-sea CO_2 gas exchange. Global Biogeochemical Cycles, 20(3): GB3020, doi: 10.1029/2005GB002491

Bates N R, Pequignet A C, Sabine C L. 2006b. Ocean carbon cycling in the Indian Ocean: 2. Estimates of net community production. Global Biogeochemical Cycles, 20(3): GB3021, doi: 10.1029/2005GB002492

Benshila R, Durand F, Masson S, et al. 2014. The upper Bay of Bengal salinity structure in a high-resolution model. Ocean Modelling, 74: 36–52, doi: 10.1016/j.ocemod.2013.12.001

Bonjean F, Lagerloef G S E. 2002. Diagnostic model and analysis of the surface currents in the tropical Pacific Ocean. Journal of Physical Oceanography, 32(10): 2938–2954, doi: 10.1175/1520-0485(2002)032<2938:DMAAOT>2.0.CO;2

Callaghan A H, Ward B, Vialard J. 2014. Influence of surface forcing on near-surface and mixing layer turbulence in the tropical Indian Ocean. Deep Sea Research Part I: Oceanographic Research Papers, 94: 107–123, doi: 10.1016/j.dsr.2014.08.009

Chakraborty A, Sharma R, Kumar R, et al. 2014. An OGCM assessment of blended OSCAT winds. Journal of Geophysical Research: Oceans, 119(1): 173–186, doi: 10.1002/2013JC009406

Chatterjee A, Shankar D, Shenoi S S C, et al. 2012. A new atlas of temperature and salinity for the North Indian Ocean. Journal of Earth System Science, 121(3): 559–593, doi: 10.1007/s12040-012-0191-9

Cheng Xuhua, Xie Shangping, McCreary J P, et al. 2013. Intraseasonal variability of sea surface height in the Bay of Bengal. Journal of Geophysical Research: Oceans, 118(2): 816–830, doi: 10.1002/jgrc.20075

Diansky N A, Zalesny V B, Moshonkin S N, et al. 2006. High resolution modeling of the monsoon circulation in the Indian Ocean. Oceanology, 46(5): 608–628, doi: 10.1134/S000143700605002X

de Boyer Montégut C, Durand F, Bourdallé-Badie R, et al. 2014. Role of fronts in the formation of Arabian Sea barrier layers during summer monsoon. Ocean Dynamics, 64(6): 809–822, doi: 10.1007/s10236-014-0716-7

de Boyer Montégut C, Vialard J, Shenoi S S C, et al. 2007. Simulated seasonal and interannual variability of the mixed layer heat budget in the northern Indian Ocean. Journal of Climate, 20(13): 3249–3268, doi: 10.1175/JCLI4148.1

Dube S K, Luther M E, O'Brien J J. 1990. Relationships between interannual variability in the Arabian Sea and Indian summer monsoon rainfall. Meteorology and Atmospheric Physics, 44(1–4): 153–165, doi: 10.1007/BF01026816

Durand F, Papa F, Rahman A, et al. 2011. Impact of Ganges-Brahmaputra interannual discharge variations on bay of Bengal salinity and temperature during 1992–1999 period. Journal of Earth System Science, 120(5): 859–872, doi: 10.1007/s12040-011-0118-x

Durand F, Shankar D, de Boyer Montégut C, et al. 2007. Modeling the barrier-layer formation in the Southeastern Arabian Sea. Journal of Climate, 20(10): 2109–2120, doi: 10.1175/JCLI4112.1

Foltz G R, Grodsky S A, Carton J A, et al. 2003. Seasonal mixed layer heat budget of the tropical Atlantic Ocean. Journal of Geophysical Research, 108(C5): 3146, doi: 10.1029/2002JC001584

George M S, Bertino L, Johannessen O M, et al. 2010. Validation of a hybrid coordinate ocean model for the Indian Ocean. Journal of Operational Oceanography, 3(5): 25–38

Gutzler D S, Harrison D E. 1987. The structure and evolution of seasonal wind anomalies over the near-equatorial eastern Indian and western Pacific Oceans. Monthly Weather Review, 115(1): 169–192, doi: 10.1175/1520-0493(1987)115<0169:TSAEOS>2.0.CO;2

Han Weiqing, McCreary Jr J P, Kohler K E. 2001. Influence of precipitation minus evaporation and bay of Bengal rivers on dynamics, thermodynamics, and mixed layer physics in the upper Indian Ocean. Journal of Geophysical Research: Oceans, 106(C4): 6895–6916, doi: 10.1029/2000JC000403

Holte J, Gilson J, Talley L D, et al. 2016. Argo mixed layers. San Diego: Scripps Institution of Oceanography/UCSD, http://mixedlayer.ucsd.edu [2016–11–27]

Holte J, Talley L. 2009. A new algorithm for finding mixed layer depths with applications to Argo data and Subantarctic Mode Water formation. Journal of Atmospheric and Oceanic Technology, 26(9):1920–1939, doi: 10.1175/2009JTECHO543.1

Huang Boyin, Xue Yan, Wang Hui, et al. 2012. Mixed layer heat budget of the El Niño in NCEP climate forecast system. Climate Dynamics, 39(1–2): 365–381, doi: 10.1007/s00382-011-1111-4

Huang Boyin, Xue Yan, Zhang Dongxiao, et al. 2010. The NCEP GODAS ocean analysis of the tropical pacific mixed layer heat budget on seasonal to interannual time scales. Journal of Climate, 23(18): 4901–4925, doi: 10.1175/2010JCLI3373.1

Huang Ke, Derada S, Xue Huijie, et al. 2015. A 1/8° coupled biochemical-physical Indian Ocean regional model: physical results and validation. Ocean Dynamics, 65(8): 1121–1142, doi: 10.1007/s10236-015-0860-8

Jackett D R, McDougall T J. 1995. Minimal adjustment of hydrographic profiles to achieve static stability. Journal of Atmospheric and Oceanic Technology, 12(2): 381–389, doi: 10.1175/1520-0426(1995)012<0381:MAOHPT>2.0.CO;2

Kalnay E, Kanamitsu M, Kistler R, et al. 1996. The NCEP/NCAR 40-year reanalysis project. Bulletin of the American Meteorological Society, 77: 437–471, doi: 10.1175/1520-0477(1996)077<0437:TNYRP>2.0.CO;2

Kantha L, Rojsiraphisal T, Lopez J. 2008. The North Indian Ocean circulation and its variability as seen in a numerical hindcast of the years 1993-2004. Progress in Oceanography, 76(1): 111–147, doi: 10.1016/j.pocean.2007.05.006

Keerthi M G, Lengaigne M, Drushka K, et al. 2016. Intraseasonal variability of mixed layer depth in the tropical Indian Ocean. Climate Dynamics, 46(7–8): 2633–2655, doi: 10.1007/s00382-015-2721-z

Keerthi M G, Lengaigne M, Vialard J, et al. 2013. Interannual variability of the tropical Indian Ocean mixed layer depth. Climate Dynamics, 40(3–4): 743–759, doi: 10.1007/s00382-012-1295-2

Krishnamurthy V, Kirtman B P. 2003. Variability of the Indian Ocean: relation to monsoon and ENSO. Quarterly Journal of the Royal Meteorological Society, 129(590): 1623–1646, doi: 10.1256/qj.01.166

Large W G, McWilliams J C, Doney S C. 1994. Oceanic vertical mixing: a review and a model with a nonlocal boundary layer parameterization. Reviews of Geophysics, 32(4): 363–403, doi: 10.1029/94RG01872

Large W G, Pond S. 1982. Sensible and latent heat flux measurements over the ocean. Journal of Physical Oceanography, 12(5): 464–482, doi: 10.1175/1520-0485(1982)012<0464:SALHFM>2.0.CO;2

Li Yuanlong, Han Weiqing, Lee T. 2015. Intraseasonal sea surface salinity variability in the equatorial Indo-Pacific Ocean induced by Madden-Julian oscillations. Journal of Geophysical Research: Oceans, 120(3): 2233–2258, doi: 10.1002/2014JC010647

Liu Zhengyu, Alexander M. 2007. Atmospheric bridge, oceanic tunnel, and global climatic teleconnections. Reviews of Geophysics, 45(2): RG2005, doi: 10.1029/2005RG000172

Lorbacher K, Dommenget D, Niiler P P, et al. 2006. Ocean mixed layer depth: a subsurface proxy of ocean-atmosphere variability. Journal of Geophysical Research: Oceans, 111(C7): C07010, doi: 10.1029/2003JC002157

Marshall J, Adcroft A, Hill C, et al. 1997. A finite-volume, incompressible Navier Stokes model for studies of the ocean on parallel computers. Journal of Geophysical Research: Oceans, 102(C3): 5753–5766, doi: 10.1029/96JC02775

Masumoto Y, Morioka Y, Sasaki H. 2008. High-resolution Indian Ocean simulations-Recent Advances and Issues from OFES. In: Hecht M W, Hasumi H, eds. Ocean Modeling in an Eddying Regime. Washington DC: American Geophysical Union, doi: 10.1029/177GM14

Moisan J R, Niiler P P. 1998. The seasonal heat budget of the North Pacific: net heat flux and heat storage rates (1950–1990). Journal of Physical Oceanography, 28(3): 401–421, doi: 10.1175/1520-0485(1998)028<0401:TSHBOT>2.0.CO;2

Momin I M, Mitra A K, Mahapatra D K, et al. 2014. Impact of model resolutions on Indian Ocean simulations from Global NEMO Ocean Model. Indian Journal of Geo-Marine Science, 43(9): 1667–1674

Narvekar J, Prasanna Kumar S. 2006. Seasonal variability of the mixed layer in the central Bay of Bengal and associated changes in nutrients and chlorophyll. Deep Sea Research Part I: Oceanographic Research Papers, 53(5): 820–835, doi: 10.1016/j.dsr.2006.01.012

Neetu S, Lengaigne M, Vincent E M, et al. 2012. Influence of upper-ocean stratification on tropical cyclone-induced surface cool-

ing in the Bay of Bengal. Journal of Geophysical Research: Oceans, 117(C12): C12020, doi: 10.1029/2012JC008433
Prasad T G. 2004. A comparison of mixed-layer dynamics between the Arabian Sea and Bay of Bengal: one-dimensional model results. Journal of Geophysical Research: Oceans, 109(C3): C03035, doi: 10.1029/2003JC002000
Prasanna Kumar S, Narvekar J. 2005. Seasonal variability of the mixed layer in the central Arabian Sea and its implication on nutrients and primary productivity. Deep Sea Research Part II: Topical Studies in Oceanography, 52(14–15): 1848–1861, doi: 10.1016/j.dsr2.2005.06.002
Rao R R, Sivakumar R. 2003. Seasonal variability of sea surface salinity and salt budget of the mixed layer of the North Indian Ocean. Journal of Geophysical Research: Oceans, 108(C1): 9–1–9–14, doi: 10.1029/2001JC000907
Roxy M K, Ritika K, Terray P, et al. 2015. Drying of Indian subcontinent by rapid Indian Ocean warming and a weakening land-sea thermal gradient. Nature Communications, 6: 7423, doi: 10.1038/ncomms8423
Schiller A, Godfrey J S. 2003. Indian Ocean intraseasonal variability in an ocean general circulation model. Journal of Climate, 16(1): 21–39, doi: 10.1175/1520-0442(2003)016<0021:IOIVIA>2.0.CO;2
Schott F A, McCreary Jr J P. 2001. The monsoon circulation of the Indian Ocean. Progress in Oceanography, 51(1): 1–123, doi: 10.1016/S0079-6611(01)00083-0
Schott F A, Xie Shangping, McCreary Jr J P. 2009. Indian Ocean circulation and climate variability. Reviews of Geophysics, 47(1): RG1002, doi: 10.1029/2007RG000245
Sengupta D, Bharath Raj G N, Shenoi S S C. 2006. Surface freshwater from Bay of Bengal runoff and Indonesian throughflow in the tropical Indian Ocean. Geophysical Research Letters, 33(22): L22609, doi: 10.1029/2006GL027573
Shankar D, Vinayachandran P N, Unnikrishnan A S. 2002. The monsoon currents in the north Indian Ocean. Progress in Oceanography, 52(1): 63–120, doi: 10.1016/S0079-6611(02)00024-1
Sharma R, Agarwal N, Basu S, et al. 2007. Impact of satellite-derived forcings on numerical ocean model simulations and study of sea surface salinity variations in the Indian Ocean. Journal of Climate, 20(5): 871–890, doi: 10.1175/JCLI4032.1
Sharma R, Agarwal N, Momin I M, et al. 2010. Simulated sea surface salinity variability in the tropical Indian Ocean. Journal of Climate, 23(24): 6542–6554, doi: 10.1175/2010JCLI3721.1
Sharma R, Mankad B, Agarwal N, et al. 2012. An assessment of two different satellite-derived precipitation products in relation to simulation of sea surface salinity in the tropical Indian Ocean. Journal of Geophysical Research, 117(C7): C07001, doi: 10.1029/2012JC008078
Shenoi S S C, Saji P K, Almeida A M. 1999. Near-surface circulation and kinetic energy in the tropical Indian Ocean derived from Lagrangian drifters. Journal of Marine Research, 57(6): 885–907, doi: 10.1357/002224099321514088
Smith W H F, Sandwell D T. 1997. Global sea floor topography from satellite altimetry and ship depth soundings. Science, 277(5334): 1956–1962, doi: 10.1126/science.277.5334.1956
Song Qian, Vecchi G A, Rosati A J. 2007. Indian Ocean variability in the GFDL coupled climate model. Journal of Climate, 20(13): 2895–2916, doi: 10.1175/JCLI4159.1
Stevenson J W, Niiler P P. 1983. Upper ocean heat budget during the Hawaii-to-Tahiti shuttle experiment. Journal of Physical Oceanography, 13(10): 1894–1907, doi: 10.1175/1520-0485(1983)013<1894:UOHBDT>2.0.CO;2
Subrahmanyam B, Murty V S N, Sharp R J, et al. 2005. Air-sea coupling during the tropical cyclones in the Indian Ocean: a case study using satellite observations. Pure and Applied Geophysics, 162(8–9): 1643–1672, doi: 10.1007/s00024-005-2687-6
Thadathil P, Gopalakrishna V V, Muraleedharan P M, et al. 2002. Surface layer temperature inversion in the Bay of Bengal. Deep Sea Research Part I: Oceanographic Research Papers, 49(10): 1801–1818, doi: 10.1016/S0967-0637(02)00044-4
Thangaprakash V P, Suprit K, Kumar N S, et al. 2016. What controls seasonal evolution of sea surface temperature in the Bay of Bengal? Mixed layer heat budget analysis using moored buoy observations along 90°E. Oceanography, 29(2): 202–213, doi: 10.5670/oceanog
Thompson B, Gnanaseelan C, Parekh A, et al. 2008. North Indian Ocean warming and sea level rise in an OGCM. Journal of Earth System Science, 117(2): 169–178, doi: 10.1007/s12040-008-0007-0
Thompson B, Gnanaseelan C, Salvekar P S. 2006. Variability in the Indian Ocean circulation and salinity and its impact on SST anomalies during dipole events. Journal of Marine Research, 64(6): 853–880, doi: 10.1357/002224006779698350
Thomson R E, Fine I V. 2003. Estimating mixed layer depth from oceanic profile data. Journal of Atmospheric and Oceanic Technology, 20(2): 319–329, doi: 10.1175/1520-0426(2003)020<0319:EMLDFO>2.0.CO;2
Vecchi G A, Harrison D E. 2004. Interannual Indian rainfall variability and Indian Ocean sea surface temperature anomalies. In: Wang C, Xie S P, Carton J A, eds. Earth's Climate: The Ocean-Atmosphere Interaction. Washington, DC: AGU, 247–260
Vinayachandran P N, Jahfer S, Nanjundiah R S. 2015. Impact of river runoff into the ocean on Indian summer monsoon. Environmental Research Letters, 10(5): 054008, doi: 10.1088/1748-9326/10/5/054008
Vinayachandran P N, Kurian J. 2007. Hydrographic observations and model simulation of the Bay of Bengal freshwater plume. Deep Sea Research Part I: Oceanographic Research Papers, 54(4): 471–486, doi: 10.1016/j.dsr.2007.01.007
Vinayachandran P N, Shetye S R, Sengupta D, et al. 1996. Forcing mechanisms of the Bay of Bengal circulations. Current Science, 71: 753–763
Wajsowicz R. 2002. Air-sea interaction over the Indian Ocean due to variations in the Indonesian throughflow. Climate Dynamics, 18(5): 437–453, doi: 10.1007/s00382-001-0187-7
Wang Yu, Liu Peng, Li Tianyi, et al. 2011. Climatologic comparison of HadISST1 and TMI sea surface temperature datasets. Science China Earth Sciences, 54(8): 1238–1247, doi: 10.1007/s11430-011-4214-1
Wentz F J, Gentemann C, Hilburn K A. 2015. Remote sensing systems TRMM TMI[indicate whether you used Daily, 3-Day, Weekly, or Monthly] Environmental Suite on 0.25 deg grid. Santa Rosa, CA: Remote Sensing Systems, www.remss.com/missions/tmi
Wu Renguang, Kirtman B P. 2004. Impacts of the Indian Ocean on the Indian summer monsoon-ENSO relationship. Journal of Climate, 17(15): 3037–3054, doi: 10.1175/1520-0442(2004)017<3037:IOTIOO>2.0.CO;2
Wu Lingjuan, Wang Fan, Yuan Dongliang, et al. 2007. Evolution of freshwater plumes and salinity fronts in the northern Bay of Bengal. Journal of Geophysical Research: Oceans, 112(C8): C08017, doi: 10.1029/2005JC003308